Initiation of deposition in supercritical turbidity currents downstream of a slope break

Pohl, F.[a]*, Eggenhuisen, J.T.[b], Cartigny, M.J.B.[c], and Tilston, M.C.[d]

[a] Marine School of Biological and Marine Sciences, University of Plymouth, Drake Circus, PL4 8AA Plymouth, UK

[b] Faculty of Geosciences, Utrecht University, P.O. box 80021, 3508 TA Utrecht, The Netherlands

[c] Department of Geography, Durham University, Lower Mountjoy South Road, DH1 3LE Durham, UK

[d] Department of Geosciences, University of Calgary, 2500 University Dr. T2N 1N4 Calgary, Alberta, Canada

* Corresponding author: florian.pohl@plymouth.ac.uk

Supplementary Materials are included at the end of this file.

ABSTRACT

Turbidity currents flowing across the ocean floor encounter changes of the local bathymetry including abrupt reductions in slope gradient also known as slope breaks. Turbidity currents flowing across a slope break will change their flow dynamics and may start to deposit as a consequence. Previous experiments on turbidity currents crossing a slope break have indeed observed abrupt changes of flow dynamics by the formation of a hydraulic jump, i.e., the transformation from Froude super- to subcritical flow. However, in these previous experiments the link between the flow dynamics and the onset of deposition by the flow downstream of the slope break is rather unclear due to the overall depletive and highly depositional character of the turbidity currents. In this paper, Shields-scaled turbidity currents were used to observe the flow dynamics of none-depositional supercritical flows that only started to deposit after passing a slope break. Hydraulic jumps only occurred in experiments where rapid deposition of sediment created an adverse slope downstream of the slope break, which resulted in significant deceleration and chocking of the flow. All flows crossing a slope break showed a thickness increase of the wall-region (i.e. the portion of the flow below the velocity maximum) resulting in a shear velocity decrease, which reduced the sediment suspension capacity. Estimated capacity parameters were below unity suggesting capacity-driven deposition. However, the calculated capacity parameters underestimated of the flow capacity. Because capacity-driven deposition is independent of grain size, the resulting deposits should reassemble the sediment characteristics at the flow base. The deposits in the experiments were, however, coarser and better sorted than the sediment suspended at the flow base. This discrepancy implies that both flow capacity and grain-size (competence) controlled the deposition downstream of a slope break.

INTRODUCTION

Turbidity currents are subaquatic sediment gravity flows and represent one of the most important agents for the distribution of sediment on Earth (Mutti *et al.*, 2009; Talling *et al.*, 2015). Individual turbidity currents can last for days (Azpiroz-Zabala *et al.*, 2017) and transport more sediment than the annual sediment flux of all terrestrial rivers combined (Talling *et al.*, 2007). Turbidity currents transport sediment from the continental shelf down the continental slope into the deep-marine environment, where they deposit their sediment in deep-sea fans that serve as a final sediment sink (e.g. Normark, 1970; Bouma *et al.*, 2012). Deep-sea fans hold reservoirs for natural resources such as hydrocarbons (Pettingill, 2004; Nilsen *et al.*, 2008), mineral ores, and rare-earth elements (Kato *et al.*, 2011; Hein *et al.*, 2013). More recently, deep-sea fans are shown to accumulate large quantities of organic matter (Galy *et al.*, 2007; Hage *et al.*, 2020) and serve as a sink for man-made pollutants such as plastics (Pohl *et al.*, 2020b). Understanding the transportation and deposition mechanisms of turbidity currents, especially the onset of deposition, is of key interest to predict the distribution of turbiditic sediment and any other material on the ocean floor.

Turbidity currents that flow down the relatively steep continental slope are usually none-depositional or bypassing (e.g. Stevenson *et al.*, 2015). Upon reaching the most distal part of the continental slope the flow continues on a much more gently dipping abyssal plane. This transition is typically marked by a slope break, i.e. a reduction in slope gradient, which affects the flow dynamics and often result in sediment deposition (e.g. Mutti & Normark, 1987). The impact of a slope break on turbidity current dynamics and deposits has been addressed in a number of laboratory experiments (Garcia & Parker, 1989; Garcia, 1993, 1994; Marr *et al.*, 2001; Mulder & Alexander, 2001; Gray *et al.*, 2005, 2006; Toniolo *et al.*, 2006; Islam & Imran, 2010; Pohl *et al.*, 2020a) and in numerical studies (Choi & Garcia, 1995; Kostic & Parker, 2006, 2007; Cantero *et al.*, 2014).

These studies show contrasting relations between the decrease in slope gradient and the dynamics and depositional signature of the turbidity currents. The Froude-scaled, but highly depletive, turbidity currents in some experiments were unable to bypass their sediment load even on the steep slopes upstream of the slope break, making it difficult to investigate the slope-break-induced transition from bypass to deposition.

For example, the slope-break experiments of Garcia & Parker (1989) revealed no impact of the slope break on the deposit thickness, despite the formation of a hydraulic jump (i.e. the transition from supercritical to subcritical flow). A hydraulic jump results in enhanced turbulence that could give the flow an increased erosion potential and thinner deposits (Komar, 1971; Chanson, 2004). However, a hydraulic jump is a local phenomenon and the subcritical flow downstream of the jump is thicker, slower, and no longer able to keep all sediment in suspension, resulting in high sediment fallout rates and thicker deposits (e.g. Dorrell *et al.*, 2016). Consequently, hydraulic jumps are associated with sediment deposition downstream of a slope break (e.g. Mutti & Normark, 1987; Lee *et al.*, 2002; Brooks *et al.*, 2018), as well as with erosive structures such as scours in channel to lobe transition zones (Kenyon & Millington, 1995; Palanques *et al.*, 1996; Wynn *et al.*, 2002; Hofstra *et al.*, 2015; Dorrell *et al.*, 2016; Brooks *et al.*, 2018).

In contrast to the experiments of Garcia & Parker (1989), the experiments by Gray *et al.* (2005; 2006) revealed the absence of a hydraulic jump and a decrease in deposit thickness downstream of the slope break. Therefore, the authors provided an alternative mechanism to the hydraulic jump to explain observed decrease in deposit thickness. In their model, excess turbulence was produced due to the slope break, enabling the turbidity current to maintain more sediment in suspension, and thus enhance sediment transport downstream of the slope break (Gray *et al.*, 2005, 2006). Increased turbulence production by a slope break was later also demonstrated in supercritical turbidity currents (Islam & Imran, 2010). However, Islam & Imran (2010) did not provide results of any deposition from these flows.

Mulder and Alexander (2001) studied the deposits of turbidity currents crossing a slope break with steeper slopes and higher sediment concentrations. The experiments revealed, in contrast to the decrease in deposit thickness of previous studies, an increase in deposit thickness downstream of the slope break. The increase in deposit thickness was explained as a result of a deceleration of the turbidity current on the gentler slope and a change of the turbulence intensity of the flow (Mulder & Alexander, 2001).

In summary the contrasting results presented in the literature demonstrate that both the flow dynamics and the depositional signal of a turbidity current crossing a slope break are still a subject of debate. Previous experiments have used Froude-scaled turbidity currents that correctly reproduce the flow dynamics of turbidity currents crossing a slope break, but are unable to maintain a non-depositional state even on the steeper sections upstream of the slope break. More recently Shields-scaling has been applied to turbidity currents to scale both the flow dynamics as well as the sediment dynamics (de Leeuw *et al.*, 2016). This paper presents flume experiments with Shields-scaled turbidity currents to simultaneously observe the flow dynamics and the resulting sediment deposition as an initially non-depositional turbidity current crosses a slope break. These experiments enable us to investigate the dynamics of turbidity currents associated to the onset of deposition at the slope break. The slope upstream and downstream of the break could be varied in steepness. This set-up enabled us to study how different slope break geometries control the transition from bypass to deposition. Three main research questions will be addressed: (i) What are the flow processes that control the onset of deposition downstream of a slope break? (ii) How is the depositional style of the turbidity current reflected in the depositional pattern? (iii) When does a slope break trigger the formation of a hydraulic jump?

METHODS

Experimental setup and scaling

To study the effect of a slope break on a bypassing turbidity current, the flows in the experiments need to bypass sediment on the incoming upper slope, upstream of the slope break. Shields scaling was used to generate such non-depletive, bypassing turbidity currents (sensu de Leeuw *et al.*, 2016). Briefly, Shields scaling enforces two scaling parameters that are kept close to values encountered in real-world systems: The boundary Reynolds number, describing the hydraulic roughness condition of the sublayer, and the Shields parameter, which is the ratio between shear stress and the gravity force acting on particles (Shields, 1936). This scaling approach generates relatively dense turbidity currents on steep slopes that can either bypass or deposit, solely based on morphologic changes in the experiment setup (de Leeuw *et al.*, 2016, 2018a; b; Pohl *et al.*, 2019, 2020a; Fernandes *et al.*, 2020; Spychala *et al.*, 2020). A more specific description of the Shields scaling methodology, in particular for the experimental setup used for this study, can be found in Pohl *et al.* (2020a).

An elongated flume tank (4 m long x 0.5 m high x 0.22 m wide) filled with fresh-water was separated into an upper slope segment of 1.7 m and a lower slope segment of 1.8 m separated by a slope break (Fig. 1). The gradient of both slope segments could be varied independently resulting in 14 experimental runs of which each had a different slope-break geometry (Table 1). Fine-grained poorly-sorted sediment (d_{16}: 57 µm, d_{50}: 133 µm, d_{84}: 194 µm; φ = 1.2; Fig. S1) was glued to the floor of the slope segments to create a rough surface to meet the Shields scaling requirements. A longitudinally oriented separation wall subdivided the flume tank into two, 0.1 m wide channels (see inset view in Fig. 1) minimizing the backflow effect that is generated in flumes to balance the ambient water that is dragged downstream at the top interface of the turbidity currents. The turbidity currents flowed in one of these channels leaving the other channel to replenish the fresh water without introducing additional friction.

At the downstream side of the flume tank was an expansion tank (3 m x 2 m x 1.8 m), where flows spread laterally, decelerated and dissipated (Fig. 1).

To create the turbidity current, a mixture of sediment and fresh water with a volume of 0.45 m^3 was prepared in a separate mixing tank (Fig. 1). The sediment density was 2,650 kg m^{-3} and the grain size was the same as used for the floor of the slope segments. The sediment concentration of the initial mixture was set to 17% vol to meet the Shields scaling requirements. The mixture was released on the upper slope segment through an inlet box (Fig. 1). The discharge was set to 12.5 m^3 h^{-1} monitored with a discharge meter (Krohne Optiflux 2300) and resulted in a current velocity of ~0.8 m s^{-1} at the inlet box and a flow duration of ~100 s. At the end of an experiment, emptying of the mixing tank resulted in a decrease in discharge and a waning turbidity current that deposited a 7 – 10 mm thick sediment layer over the entire length of the flume.

Pohl et al 2020b analysed an extensive range of combinations of upper and lower slopes. This paper focuses on the flow dynamics of a subset of those experiments. Pohl et al. 2020b established that bypass conditions in this set-up were achieved at slopes equal to or steeper than 6°. This paper therefore focusses on the experiments with an upper-slope segment of 6° and 8°. The lower slope segment was varied between 0° and 8° degrees to trigger the deposition from the turbidity current downstream of the slope break. The experiments include two geometrical setups without a slope break between the upper and lower slope segment (Run 7 and 14; Table 1).

Data acquisition

UVP measurements

The velocity of the turbidity currents was recorded with an Ultrasonic Doppler Velocimetry Probe (UVP). The UVP was deployed on the lower slope at 2.3 m downstream of the inlet box, elevated 0.11 m above the bed, and facing the upstream direction at an angle of α = 60° relative to the local bed (Fig. 2a). The UVP emitted an ultrasonic sound signal at a frequency of 1 MHz that was reflected back to the UVP by the suspended sediment grains. Here, grain motions cause a frequency shift of the reflected signal due to the Doppler-effect which yielded the velocity of the grains. Detailed UVP acquisition settings are provided in Table S1. Further information on the functions and limitations of UVPs can be found in Takeda, (1995) and in Lemmin & Rolland, (1997).

An inclined UVP measures the velocity along the direction aligned with the orientation of the UVP (u_p; Fig. 2a). Pilot experiments with a bed-normal oriented probe showed that the bed-normal velocitycomponent of the flows is close to zero and can be neglected. Thus, the bed-parallel velocity component (u_x) can be calculated with (Cartigny *et al.*, 2013; Sequeiros *et al.*, 2018):

$$u_x = u_p / \cos(\alpha) \quad . \tag{1}$$

This results in an instantaneous velocity profile $u(z)$ of the flow, with z as the bed-normal coordinate (Fig. 2b).

The distance between the UVP and the bed is sometimes decreased over time due to sediment aggradations underneath the probe. This reduction in distance was tracked over time to correct the bed-normal coordinate (z) (Fig. S2). The instantaneous velocity profiles were averaged over time to obtain a smooth appearance. An averaging window was set to only collect velocity profiles within the main body of the flow. The velocity was averaged over a period of ~80 s. The start of the averaging window was set ~20 s after the current head passed the UVP probe. The averaging window stopped before the current tail was deposited.

The time-averaged velocity profiles were used to obtain the flow velocities and dimensions of the turbidity currents (Fig. 2b). The flow thickness (h) is defined here as the height at which the velocity $u(z)$ is half the velocity maximum (u_m) (following Launder & Rodi, 1983; Kneller & Buckee, 2000; Buckee *et al.*, 2001; Gray *et al.*, 2005). The height of the velocity maximum above the bed is h_m and divides the turbidity current into two regions (e.g. Altinakar *et al.*, 1996; Kneller *et al.*, 1999; Eggenhuisen & McCaffrey, 2012). This paper refers to the region below h_m as the wall-region, with thickness h_w, and to the region above h_m as the mixing-region, with thickness h_{mx} (Fig. 2b).

Siphon samples

The turbidity current was siphoned to measure sediment concentration and grain-sizes of sediment suspended at different elevations. Four siphon tubes were deployed 2.5 m downstream of the inlet box at different elevations above the flume-tank floor (0.01, 0.02, 0.04, and 0.08 m) (Fig. 1). Siphon tube diameter was 7 mm and the average flow velocity in the siphon tubes was approximately 1 m s^{-1}. To measure the sediment concentration on the upper slope segment, additional duplicate experiments have been conducted with the siphon tubes installed on the upper slope segment, 1.4 m downstream of the inlet box. Siphoning commenced ~20 s after the start of an experiment, after the current head had passed the siphon tubes, and was continued until either 2 liters of mixture was sampled, or until the lowermost siphon tube was buried by aggrading sediment. The volume and weight of the sample of each siphon tube was measured. Sediment concentration was then calculated from the bulk density of the siphon sample and the specific densities of the water (1,000 kg m^{-3}) and the suspended sediment (2,650 kg m^{-3}). The sediment captured by the siphon tubes was analyzed for its grain size using laser diffraction (Malvern Mastersizer 2000, Malvern Instruments Limited, Malvern, UK). In some instances, the siphoned sediment volume was too low for the laser diffraction, and no reliable grain-size distribution could be obtained.

Flow parameterization

The shear velocity u_* is used to describe the turbulent shear at the base of the flow and is related to the bed shear stress. The shear velocity is a key variable in the evaluation of the sediment transport capability of a flow (e.g. Rouse, 1937; Eggenhuisen *et al.*, 2017). Here, the shear velocity is estimated by assuming a logarithmic velocity profile between the bed and the velocity maximum u_m (following Middleton & Southard, 1984; van Rijn, 1993; Cartigny *et al.*, 2013; de Leeuw *et al.*, 2016; Pohl *et al.*, 2019):

$$u_* = u_\mathrm{m}\kappa\left(\ln\left(\frac{h_\mathrm{m}}{0.1d_{90}}\right)\right)^{-1}, \tag{2}$$

where κ is the von Kármán constant with a value of 0.4. The d_{90} of the initial sediment distribution was 215 µm.

The maximum sediment concentration that a turbidity current can contain in suspension is here referred to as the suspension capacity (Kuenen & Sengupta, 1970). The suspension capacity parameter Γ gives a theoretical capacity limit at the base of a turbulent flow (Eggenhuisen *et al.*, 2017):

$$\Gamma = \frac{u_*^3}{140\nu g\left(\frac{\rho_s-\rho_w}{\rho_w}\right)C_b}, \tag{3}$$

where ν is the kinematic viscosity of water ($1 \cdot 10^{-6}$ m² s^{-1}, at a temperature of 20°C), ρ_w is the density of water (1,000 kg m^{-3}), ρ_s the density of the quartz sand (2,650 kg m^{-3}), and C_b is the sediment concentration at the base of the flow. The capacity parameter is the ratio of the vertical turbulent forces acting close to the bed, and the gravity force acting on suspended particles per unit volume. The capacity criterion Γ = 1 describes the theoretical capacity limit of the flow. For Γ < 1 the flow is 'over capacity'; turbulence will no longer be generated near the bed, and sediment will be deposited. Γ > 1 describes a flow that is 'under capacity' and sediment is kept in suspension and may be eroded and entrained from the bed. The sediment concentration measured from the lowest siphon tube is used to calculate capacity parameter values for the experiments

The densiometric Froude number *Fr´* is a dimensionless number that compares the kinematic and potential energy scales of the flow. *Fr´* > 1 describes a supercritical flow and *Fr´* < 1 a subcritical flow. A hydraulic jump forms at a transition from supercritical to subcritical conditions (*Fr´* ≈ 1) (e.g. Wood, 1967; Komar, 1971; Weirich, 1988). *Fr´* is calculated as:

$$Fr' = \frac{U}{\sqrt{g'h}} \ , \tag{4}$$

where U is the depth-averaged velocity of the flow and $g´$ is the submerged gravity that accounts for the buoyancy of the ambient fluid. The submerged gravity is defined as:

$$g' = g\,\frac{(\rho_t - \rho_w)}{\rho_t} \ , \tag{5}$$

where g is the constant acceleration by gravity (9.81 m s^{-1}) and ρ_t is the density of the turbidity current:

$$\rho_t = C\rho_s + (1 - C)\rho_w \ , \tag{6}$$

where C is the depth-averaged sediment concentration of the turbidity current.

Deposition pattern and deposit sampling

The thickness of the deposits was manually measured through the glass side-wall at longitudinal intervals of 0.05 m. In all experiments that yielded a deposit, the deposit thickness decreased rapidly over the final ~0.35 m of the flume. This rapid thinning of the deposit was an artifact of the transition from the flume into the expansion tank.

The flume was slowly drained, to expose and sample the deposits. Prior to sampling, the upper ~7 – 10 mm of the deposits, which were deposited by the starved turbidity current towards the end of the experiment, were scraped off to expose the deposits of the main body of the flow. Because the siphon tubes will induce turbulence during the experiments and thus disturb the downstream deposits, the deposits were sampled 0.1 m in front of the siphon tubes (i.e. 2.4 m downstream of the inlet box). The samples were analyzed for their grain size by laser diffraction (Malvern Mastersizer 2000, Malvern Instruments Limited, Malvern, UK).

RESULTS

Deposition patterns

Variation of the slope geometry resulted in a variety of different flow behaviors ranging from bypass to deposition. In both experiments without a slope break the turbidity currents were bypassing (Run 7 and 14; Fig. 3). Turbidity currents flowing over a slope break generally bypassed on the upper slope segment and deposited on the lower slope segment if the gradient of the lower slope segment was less than 5°. A further decrease of the gradient of the lower slope segment led to thicker deposits (Fig. 3). Turbidity currents in the experiments with a horizontal lower slope segment showed a different deposition pattern due to the development of a hydraulic jump which is described in section ‘Flow parameters’, below. The deposition rate of the turbidity current downstream of the hydraulic jump increased significantly, resulting in thick deposits on the lower slope segment and also deposition on the upper slope segment (Fig. 3).

Flow dynamic measurements

Flow velocities and dimensions

The flow velocities and dimensions of the turbidity currents were controlled by the geometry of the slope break system where the steepness of the slope-break angle appears to be the main factor. Flows in experiments with the steeper upper slope segment of 8° were faster than flows in experiments with the more gently dipping upper slope segment of 6° (Table 2 and Fig. 4). Both depth-averaged flow velocity (U) and the velocity maximum (u_m) showed a slight decrease with the increase of the slope-break angle (Figs. 4a and b). The depth-averaged velocity in the wall-region (U_w) showed a stronger decrease with an increasing slope-break angle (Fig. 5c). Downstream of the slope break, the turbidity current was thickening at a magnitude correlating with the slope-break angle (Fig. 5d). Flow thickening was mainly due to a thickness increase of the wall-region (h_w), while the thickness of the mixing-region (h_{mx}) remained constant with an increasing slope-break angle (Figs. 5e and f).

Sediment stratification

The density profiles of the turbidity currents generally showed a stratification with a decreasing density towards the top of the flow (Fig. 4b). The profiles obtained from the siphon samples collected upstream of the slope break, 1.4 m downstream from the inlet box, showed the lowest degree in vertical stratification (see dashed line in Figure 4b). At the sampling location on the lower slope segment, 2.5 m downstream from the inlet box, the density stratification was increased. When the turbidity current crossed a slope break, the vertical density stratification was decreased at a magnitude that correlates to the steepness slope-break angle (Fig. 4b). A steeper slope-break angle resulted in a less stratified turbidity currents.

Sediment grain-size and sorting

Generally, the grain-size of the sediment suspended in the turbidity currents was coarser towards the flow base (Fig. 6a). The degree in vertical downward coarsening showed only a minor response to the slope-break angle, but turbidity currents appear to be coarser grained in experiments with a steeper slope-break angle (Fig. S4). However, a clear correlation between the slope-break angle and the grain-size stratification of the flow could not be recognized.

The grain-size distribution of the deposits was coarser than that of the sediment sampled from the lowermost siphon tube at 1 cm above the bed (Fig. 6a). Relative to the grain-size distribution from the lowermost siphon tube, the grain-size distribution of the deposits was coarser. This was a result of a decrease of the fine grain fraction (<90 µm) and a slight increase of the coarser grain fraction (>150 µm).

The sediment sorting of the grain-size distribution was calculated by the moment method following Boggs (2009). The Phi standard deviation (ϕ) of the sediment suspended in the turbidity current was between 1.0 to 1.4 and thus poorly sorted (Fig. 6b and Table 3). Within the turbidity currents, sediment sorting was increasing toward the flow base, although there was no correlation between the vertical stratification in sorting and the slope-break geometry identifiable. The sediments of the deposits were moderately sorted with a Phi standard deviation between 0.7 and 0.8 and thus, better sorted than the sediment in the turbidity current (Fig. 6b).

Flow parameters

Shear velocity

Calculated shear velocities u_* varied between 0.06 to 0.07 m s^{-1} (Table 4). Shear velocities were generally higher in the experiments with the upper slope segment of 8° than in the experiments with the more gently dipping upper slope segment of 6° (Fig. 7a). In addition, the shear velocity was controlled by the slope-break angle, where shear velocities decreased proportionally to an increasing slope-break angle (Fig. 7b). Decrease in shear velocity relative to the setup with no slope break, was up to 3% in experiments with an upper slope segment of 6°, and up to 9% in experiments with an upper slope segment of 8°.

Capacity criterion

The calculated capacity parameter Γ was below unity in all of the experiments indicating that all flows were over-capacity (Table 4). The capacity parameter indicated stronger over-capacity in experiments with the steeper upper slope segment of 8° compared to experiments with the more gently dipping upper slope segment of 6° (Fig. 7c). The capacity parameter was generally decreased when the turbidity current was passing a slope break, with a magnitude corresponding to the slope-break angle (Fig. 7d).

Densiometric Froude number

Calculated densiometric Froude numbers *Fr´* show that the turbidity currents were within the supercritical flow-regime in all experiments (Table 4). Froude numbers were generally higher in experiments with the steeper upper slope segment of 8° (Fig. 8a). In experiments with a slope break, the Froude numbers on the lower slope segment decreased with the magnitude of the slope-break angle (Fig. 8b).

These results show that Froude numbers remained above unity and no hydraulic jump occurred. However, exceptions are the two experiments with a horizontal lower slope segment (Run 1 and 8; cf. Table 1) in which a roller structure occurred. In these experiments deposition of sediment on the horizontal lower slope segment generated a ramp with an adverse gradient, resulting in significant deceleration of the flow as it had to flow upslope. A roller structure developed at the thickest point of the accreted sediment and propagated upstream during the last ~10 to 20 s of the experiment (Fig. S5a). It was not possible to calculate Froude numbers based on the collected data over the last seconds of the experiments when the roller structure was active. The reason is that the assumption of bed-parallel mean velocities of the turbidity current is not valid for the roller structure, where particles were transported mainly in the bed-normal direction (Fig. S5a, and supplementary material video 2). In other experiments on steeper slopes, with higher flow velocities and less deposition, no roller structure could be observed (Figs. S5b, c, and supplementary material Videos 3 and 4).

DISCUSSION

Flow transformation and deposition at a slope break

Flow thickening

Our results show that the turbidity currents were thickening downstream of the slope break at a magnitude that correlates with the slope-break angle (Fig. 5d). A turbidity current flowing across a slope is driven by the tangential (i.e. downslope) component of the gravity force acting on the flow. When that turbidity current crosses a slope break, the abrupt decrease in the slope gradient immediately reduces the tangential component of the gravity force. This results in deceleration of the flow due to the friction with the ambient fluid and the flume-tank floor (e.g. Altinakar *et al.*, 1996; Kneller *et al.*, 1999). Deceleration, in turn, results in thickening of the turbidity currents due to the conservation of mass. In addition, flow thickening is also caused by entrainment of ambient water at the top of the flow. However, in the experimental turbidity currents flow thickening was predominantly noticeable for the wall-region (h_w), and thus accompanied by an increase in the height of the velocity maximum (h_m) (Fig. 5e). The thickness and structure of the mixing layer (h_{mx}) remains virtually unchanged because the maximum velocity is not changing (Fig. 5f).

Density stratification and turbulence production

The turbidity currents in the experiments develop a vertical density stratification, which increases as the currents flow through the flume tank (Fig. 4b). Density stratification is less developed when the turbidity current has crossed a slope break and development of the density stratification is suppressed with a magnitude correlating with the slope-break angle (Fig. 4b). The less developed density stratification indicates a better vertical mixing of the suspended sediment, and hence suggests an increase in turbulence due to the slope break (Fig. 9). An increase of the turbulent kinetic energy in turbidity currents crossing a slope break has been demonstrated in previous studies (Gray *et al.*, 2005, 2006; Islam & Imran, 2010). This excess turbulent kinetic energy is produced downstream of the slope break together with the decrease of the mean streamwise flow velocity (Gray *et al.*, 2005). Steel et al. (2017) argued that Taylor-Görtler vortices can be generated in turbidity currents that flow across a break of slope. Such vortices arise due to centrifugal effects when a flow with a high-velocity core is forced around a bend. Such Taylor-Görtler vortices could be the structures responsible for the inferred increased turbulence production. Previous studies have suggested that this excess turbulence delays deposition, or even causes erosion (Gray *et al.*, 2005, 2006; Islam & Imran, 2010). Though the mixing effect of increased turbulence could be recognized in our results, it was apparently not strong enough to prevent deposition downstream of the slope break.

Did the decrease of shear velocity trigger capacity-driven deposition?

The decrease in the slope gradient reduces the tangential component of the gravitational force acting on the turbidity current. This reduction causes an elevation of the height of the velocity maximum and a decrease of the velocity gradient at the base of the flow, resulting in a reduction in shear velocity (Figs. 7a, b, and 10). Lower shear velocities will decrease the sediment transport capacity of the turbidity current, resulting in deposition (Hiscott, 1994; Kneller, 2003; Dorrell *et al.*, 2013; Eggenhuisen *et al.*, 2017). Calculated suspension capacity parameters indeed decrease with a magnitude corresponding to the slope-break angle (Fig. 7d). However, capacity parameters were always below unity, even in the two experiments without a slope break in which no deposition was observed. This indicates that the capacity parameter is underestimated in this study, which may be the result of the inaccuracy in the flow parameters used for the calculation of the capacity parameter, and/or from a deficiency in the theoretical prediction of suspension capacity.

The method used to calculate the shear velocities is based on the assumption of a logarithmic velocity profile between the bed and the velocity maximum (Middleton & Southard, 1984;

van Rijn, 1993). Kneller *et al.* (1999) demonstrate that the velocity of turbidity currents is lower than that predicted from the logarithmic law of the wall, even below the velocity maximum. This deviation of the velocity profile from the assumed logarithmic profile-shape results in an underestimation of the shear velocities for turbidity currents by equation 2, and in turn an underestimation of the capacity parameter for these experiments. The concentration used to calculate the capacity parameter in this study is an additional source of error. The concentration obtained from the lowermost siphon tube, elevated 1 cm above the flume tank floor, was used as the sediment concentration at the base of the turbidity current (C_b). This resulted in an underestimation of the basal sediment concentration of ~10% vol, as implied by the sediment concentration profiles (Fig. 4b). This results in an overestimation of the calculated capacity parameter. The combined effects of uncertainty in concentrations and shear velocity estimations are not clear, though their opposite effect on capacity parameter accuracy suggests that the effect could be small. Calculation of the capacity parameter considering 10% higher shear velocity values together with basal sediment concentrations increased by 10% vol, results in a ~10% decrease of the calculated capacity parameter.

Another reason for the inaccuracy of the capacity parameter might be that the grain size of the suspended sediments plays a more important role than suggested by Eggenhuisen *et al.* (2017). These authors report that their suspension parameter becomes inaccurate if the grain size of the suspended particles is larger than 200 µm, resulting in deposition even when the capacity limit is not reached.

During capacity driven deposition, all sediment at the base of the flow would be deposited regardless of its grain size. Thus, the grain-size distribution of the deposits should reassemble the grain-size distribution at the flow base. In our experiments, the grain-size distribution in the deposits is coarser than the sediment sampled 1 cm above the flume-tank floor (Fig. 6a). Differences in grain-size distribution between the flow and the deposits mainly affected the fine grain-size fraction (<90 µm) which was less abundant in the deposits. The decrease of the fine grain-size fraction was also reflected in the sediment sorting resulting in a better sorting of the deposits (Fig. 6b).

There are three explanations for the discrepancy of the grain-size distribution between the flow and the deposits: (i) The sediment sample of the lowermost siphon tube does not accurately resemble the sediment that was suspended at the flow base. Siphon sampling showed that the vertical grain-size distribution in the turbidity current was coarsening towards the flow base (Fig. 6a). The lowermost sample from the turbidity current was taken at 1 cm above the flume-tank floor. Following the general downward coarsening trend as seen in Figure 6a, the sediment at the flow base might have been coarser than the sediment sampled at 1 cm above the flume-tank floor. (ii) Another possibility is that siphoning of a turbidity current results in a bias towards a finer grain-size distribution. Suspended sediment and interstitial water are sucked into the siphon tubes as the turbidity current passed by. Flow velocity in each of the siphon tubes was at approximately 1 m s^{-1}, which roughly corresponds to the maximum velocity of the flow at a height of ~0.02 m above the flume-tank floor. However, flow velocities above and below the velocity maximum were slower. Hence, the siphon tubes effectively extracted sediment and interstitial water at a discharge higher than that of the turbidity current at the height of the particular siphon tube. This process might result in a sampling bias towards finer grains, as these were easier to mobilize due to their lower mass and inertia. An additional siphoning artefact could be caused by the curvature in the density gradient, which makes it more easy for material to be siphoned from the top of the siphon tube compared to the bottom of the siphon tube, especially in the lowermost siphon location. The net results of these effects on the uncertainty of concentration measurements with siphon tubes is not known. (iii) The third explanation is that deposition was also controlled by the grain-size and settling velocity of the suspended sediment. Coarser grains have a have a higher mass to surface ratio and therefore settle faster than finer grains. This would increase the likelihood of deposition of coarse grains and decrease the likelihood of deposition of finer grains. This process is also known as competence-driven deposition (*sensu* Kuenen & Sengupta, 1970; Hiscott, 1994). This deposition mechanism would result in coarser grained deposits and a relative decrease of the fine grain-size fraction in relation to the sediment suspended in the flow; similar to the observations in our experiments.

In summary the causal mechanism for deposition following a slope break was a decrease in shear velocity, which caused a reduction in the transport capacity of the turbidity current. The observed transition to deposition occurred at estimated capacity parameter values of 0.6 - 0.8 (Table 4 and Fig. 7c), while the theory of Eggenhuisen *et al.* (2017) predicts this transition at 1.0. Considering the difficulty in constraining the capacity parameter with measurements from experiments, this deviation between theory and experiment can be considered a reasonably successful test. However, deposition in our experiments could also have been determined by the grain size of the sediment and finer grains appeared to be less prone to be deposited than coarser grains, resulting in deposits coarser than the sediment at the lowermost siphon location. Hence, the competence of the flow seems to be an additional deposition mechanism to the overcapacity of the flow. In any case, the underlying process initiating deposition was the decrease in shear velocity due to the slope break.

Hydraulic jumps at a slope break

No hydraulic jump due to the slope break

The depth-averaged densiometric Froude number decreased with a magnitude corresponding to the slope-break angle (Fig. 8b). The decrease of the depth-average Froude number was not sufficient to generate a hydraulic jump. If Froude numbers are far above unity, even a significant decrease of the slope-break angle will not result in a Froude number below unity, and hence no hydraulic jump will emerge. Thus, hydraulic jumps were not the primary cause for the transformation from bypass to deposition in our experiments.

The slope break experiments of Garcia (1993) include some supercritical turbidity currents that traversed a slope break without the formation of a hydraulic jump. Garcia (1993) used sediment of four different grain sizes and hydraulic jumps were absent in experiments with grains larger than 30 µm. A possible reason for the absence of a hydraulic jump might have been that the lower slope segment was too short, meaning that a hydraulic jump would have formed farther downstream (Garcia, 1993; Kostic & Parker, 2007). This explanation for the absence of a hydraulic jump in most of our experiments cannot be ruled out, although the lower slope segment in the experiments of Garcia (1993) was horizontal, whereas the lower slope segment was inclined in our experiments.

Kostic & Parker (2007) showed in numerical simulations based on the experiment of Garcia (1993) that under certain conditions supercritical turbidity currents can traverse a slope break and remain supercritical until they dissipate. In this scenario, rapid sediment deposition from the turbidity current reduces the flow density resulting in an increasing densiometric Froude number, maintaining supercritical flow conditions. In the experiments of Garcia (1993), this scenario was met for turbidity currents with grain sizes larger than >30 µm (Garcia, 1993; Kostic & Parker, 2007). In our experiment, however, also non-depositional flows remained supercritical and highly depositional flows showed a decrease in the densiometric Froude number rather than an increase (Figs. 7a and b).

As discussed in the previous section, deposition was initiated by a thickening of the wall-region and an associated decrease in shear velocity (Fig. 9). However, the observed thickness increase in combination with a decreasing velocity of the wall-region might result in subcritical flow conditions in the wall-region. This subcritical wall-region would be overlain by a supercritical mixing region resulting in a twin-layer flow behavior as observed in saline underflows in the Black Sea (Dorrell *et al.*, 2016). Unfortunately, it was not possible to calculate densiometric Froude numbers for the wall-region, due to measurement limitations of the exact flow density and velocity close to the bed. Nevertheless, the observed decrease in shear velocity in combination with the increase turbulence – as inferred from the decreasing density stratification – might be a result of a hydraulic jump restricted to the wall-region of the flow. The sediment transport capability of the subcritical wall-region is likely to be reduced, resulting in deposition.

Based on numerical simulations, Salinas *et al.* (2020) proposes the existence of transcritical flows, marked by a cyclic pattern of soft transitions between super and subcritical flows. These transitions are not marked by the occurrence of hydraulic jumps, but by the formation of instabilities, an increase in turbulence and flow thickness, and eventually the onset of deposition (Salinas *et al.*, 2020). Although the occurrence of a transcritical flow could explain the overall flow thickening and the onset of deposition in the experiments, it would not result in the observed elevation in height of the velocity maximum above the bed, and the associated thickening of the boundary layer (Figs. 5e and 9).

Hydraulic jumps due to accreting sediment and flow choking

In two experiments with a horizontal lower slope segment, a roller structure emerged during the last seconds of the experiment (Fig. S5a, and supplementary material videos 1 and 2). Unfortunately, it was not possible to capture Froude number values of the flow in the roller structure (see section 'Flow parameters'). However, hydraulic jumps in turbidity currents show a roller structure that is similar to the surface rollers generated in open-channel hydraulic jumps (e.g. Rajaratnam, 1967; Komar, 1971; Long *et al.*, 1991; Vellinga *et al.*, 2018). Therefore, the roller structure is interpreted as a hydraulic jump caused by the deceleration of the current, and a decrease of the Froude number below unity.

The hydraulic jump emerged due to deposition on the lower slope, generating a ramp with an adverse slope, dipping upstream (Fig. 10). The adverse slope caused a deceleration and thickening of the supercritical flow since it had to flow upslope. Flow deceleration culminated in the emergence of a hydraulic jump, which migrated upstream until the end of the experiment (Video 1 and 2 in the supplementary material). Hence, the accretion of sediment on the lower slope segment, rather than the slope break, is inferred to be the primary cause for the hydraulic jump in these experiments. This finding is supported by Huang *et al.* (2009), who observed in their numerical model of flows going over a slope break, the formation of hydraulic jumps in geometries with an adverse lower slope segment (see their Fig. 2).

Hamilton *et al.* (2015) found, in their experiments on autogenic avulsion cycles on submarine fans, deposition of a mouth bar at a channel outlet. This mouth bar represented an obstacle and the flows leaving the channel outlet started to choke, which culminated into a hydraulic jump (Hamilton *et al.*, 2015). Flow choking due to deposition is also proposed as a process occurring at the channel outlet in the Golo Fan in the Quaternary east Corsica Trough (Hamilton *et al.*, 2017). However, the authors also set forth that larger-scale elements in the Golo Fan (i.e. lobe complexes) that develop on lower gradients may be related to subcritical flow conditions and backwater (Hoyal & Sheets, 2009), rather than to flow choking and the formation of a hydraulic jump.

In an outcrop study, flow choking was speculated as a trigger for the formation of a hydraulic jump on the Mizala Fans in the Sorbas Basin, SE Spain (Postma & Kleverlaan, 2018). The authors describe that channel extension and lobe aggradation in the Mizala Fan culminated into flow choking at the channel outlet due to aggraded lobe sediments, and resulted in the formation of a strong hydraulic jump (Postma & Kleverlaan, 2018). This scenario is comparable to the situation observed in our experiments. Therefore, it is proposed that the formation of a hydraulic jump represents a later stage in the evolution of a slope-break system, characterized by sediment accretion and flow choking, rather than a direct primary result of the slope break (Fig. 10).

Hydraulic jumps are also interpreted as a major process related to the formation of plunge pools (Lee *et al.*, 2002; Bourget *et al.*, 2011). Lee *et al.* (2002) describe in their 'hydraulic jump pool' process-model that a hydraulic jump forms at the slope break due to the sharp decrease in slope gradient. In their model, rapid deposition downstream of the hydraulic jump forms a constructional rampart and in consequence a plunge pool morphological feature. The results of the experiments suggest that a hydraulic jump in a submarine plunge pool can also emerge because of deposition of the rampart forming an adverse slope for the flow. Hence, the hydraulic jump would emerge after the formation of the plunge pool and the depositional rampart, rather than as a direct primary result of the slope break. Revision of the process models for submarine plunge pools, regarding our additional flow dynamic mechanism for turbidity currents at the slope break, could provide new insight into the formation and preservation of submarine plunge pools.

Slope break versus loss of confinement – flow transformations in channel lobe transition zones

Slope breaks are often associated with channel lobe transitions zones (CLTZ) which are situated between the termination of a submarine canyon or channel and the onset of a sediment lobe (Mutti & Normark, 1987). The seabed in CLTZs is usually characterized by complex mixed patterns of erosive and depositional structures (Mutti & Normark, 1987; Piper & Savoye, 1993; Kenyon & Millington, 1995; Palanques *et al.*, 1996; Morris *et al.*, 1998; Nelson *et al.*, 2000; Wynn *et al.*, 2002; Habgood *et al.*, 2003; Bonnel *et al.*, 2005; Macdonald *et al.*, 2011; Ito *et al.*, 2014; Hofstra *et al.*, 2015; Brooks *et al.*, 2018). In addition to the morphological feature of a slope break, CLTZs are also defined by the loss of lateral flow confinement at the canyon or channel termination (Mutti & Normark, 1987; Wynn *et al.*, 2002). Thus, turbidity currents flowing across these zones will encounter different morphological features, each of which having its own impact on the behavior, structure, and depositional signature of the flow. A slope break results in a decrease in bed shear stress and a reduced sediment transport capability of the flow, as shown in this paper. Thus, a flow dominated by the morphological feature of a slope break would predominantly deposit sediment, which perhaps might culminate in flow choking, a hydraulic jump, and the formation of a plunge pool (e.g. Lee *et al.*, 2002; Baas *et al.*, 2004; Pohl *et al.*, 2020a). In contrast to a slope break, a flow dominated by the morphological feature of a loss of lateral confinement will trigger a mechanism called flow relaxation, leading to an increased bed shear stress and erosion (Pohl *et al.*, 2019). Thus, the loss of lateral confinement, rather than the slope break, is likely to be responsible for the erosion pattern that is commonly described in CLTZs.

A much discussed explanation for the formation of scour fields in CLTZs is the potential formation of hydraulic jumps associated with a slope break (Komar, 1971; Mutti & Normark, 1987; Garcia & Parker, 1989; Wynn *et al.*, 2002). However, it is questionable if hydraulic jumps can be responsible at all for the observed erosion in CLTZs, or even generate these zones. A hydraulic jump is the consequence of a decrease in energy and momentum of a flow usually linked to massive deposition downstream of the jump. The increased turbulence at the jump is constricted to the location at which the jump occurs, and it is unproven whether this turbulence can generate scours in the case of sediment driven gravity flows such as turbidity current. Furthermore, no study was yet able to show the formation of a hydraulic jump as a consequence of the loss of lateral confinement. It is proposed that hydraulic jumps only have a minor relevance in CLTZs and that they may emerge at pre-existing scours that were formed by previous erosive flows.

CONCLUSIONS

The Shields-scaled experiments presented in this paper could mimic the transition from bypass to deposition due to a slope break. The decrease in slope gradient reduced the downslope component of the gravity force acting on the turbidity current, resulting in deceleration and thickening of the wall-region. Thickening of the wall-region reduced the shear velocity and sediment transport capacity of the flow and caused deposition. Calculated capacity parameters of the depositional flows deviate within a factor of 2 from the theory, which underestimates the sediment transport capacity of the flow. In other words, flows that are estimated to be depositional according to the theory are in fact fully bypassing.

The grain-size distribution in the deposits was coarser and better sorted than that of the sediment suspended at the flow base. This discrepancy suggest that capacity-driven deposition is unlikely to be the only deposition style in the experiments. Hence, it is suggested that a hybrid deposition style between capacity and competence resulted in the coarser and better sorted grain-size distribution of the deposits. The grain-size distribution of the deposits reveals no dependency on the slope-break geometry.

Flows downstream of the slope break showed a lower density stratification implying a better mixing due to increased turbulence generated by the slope break. In addition, but independent of the slope-break geometry, flows showed a vertical grain-size stratification with a downward coarsening pattern. Suspended sediment was coarser towards the flow base due to a decrease of the fine fraction in the grain-size distribution, probably resulted from the lower settling velocity of finer grains. The decrease in finer grains also caused an increase of the sediment sorting toward the flow base.

Contrary to most previous experiments involving a slope break and depletive turbidity currents, no hydraulic jump emerged in the vast majority of the experiments. However, the observed thickening of the wall-region might have been caused by a hydraulic jump that was restricted to the wall-region of the flow. In experiments with a horizontal lower slope segment a roller structure emerged that was interpreted as hydraulic jump. This hydraulic jump was generated by deposits downstream of the slope break forming a ramp with an adverse slope, which resulted in flow deceleration and flow chocking, rather than because of the slope break as the primary cause. Our results provide new insights into the conception of flow dynamic models in slope-break settings involving the formation of a hydraulic jump.

The complex, joint effects of different morphological transitions in CLTZs might allow to predict different scales, styles, and morphologic evolutions of CLTZs in relation to the dominant morphological control. Systems with a steep slope-break (high slope-break angle) and a more gradual loss of confinement develop no, or smaller and less erosive CLTZs. In contrast, systems with no slope break and/or an abrupt loss of confinement are prone to the development of larger and more erosive CLTZs. A variation in the dominant morphological control through time results in a response in style and size of the CLTZ.

ACKNOWLEDGEMENTS

This contribution is part of EuroSEDS (Eurotank Studies of Experimental Deepwater Sedimentology), supported by the NWO (Netherlands Organization for Scientific Research) (grant no. NWO 864.13.006), ExxonMobil, Shell, and Equinor. The authors would like to thank Thony van der Gon Netscher and Henk van der Meer for their technical support at the Eurotank Laboratory.

DECLARATION OF INTEREST

The authors declare none.

DATA AVAILABILITY STATEMET

The data that support the findings of this study are available from the corresponding author upon reasonable request.

FIGURES

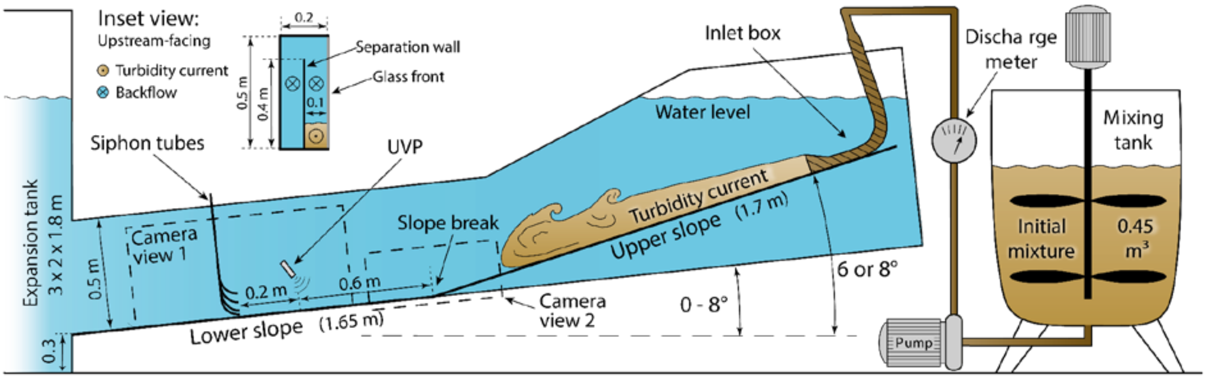

Fig. 1. Sketch of the experiment setup. The dip angle of the upper slope segment was 6° or 8° and the angle of the lower slope segment was varied between 0° to 8° (both angles with respect to the horizontal). UVP: Ultrasonic Velocimetry Probe.

Run	Input parameters						Slope-break geometry		
	Inlet velocity (m/s)	Sediment concentration (%vol)	Sediment density (kg/m³)	median grain size d_{16} (µm)	d_{50}	d_{84}	Upper slope (°)	Lower slope (°)	Slope break (°)
1	0.8	17	2,650	57	133	194	6	0	6
2	0.8	17	2,650	57	133	194	6	1	5
3	0.8	17	2,650	57	133	194	6	2	4
4	0.8	17	2,650	57	133	194	6	3	3
5	0.8	17	2,650	57	133	194	6	4	2
6	0.8	17	2,650	57	133	194	6	5	1
7	0.8	17	2,650	57	133	194	6	6	0
8	0.8	17	2,650	57	133	194	8	0	8
9	0.8	17	2,650	57	133	194	8	2	6
10	0.8	17	2,650	57	133	194	8	3	5
11	0.8	17	2,650	57	133	194	8	4	4
12	0.8	17	2,650	57	133	194	8	5	3
13	0.8	17	2,650	57	133	194	8	6	2
14	0.8	17	2,650	57	133	194	8	8	0

Table 1. Input conditions and geometrical parameters of the experimental runs.

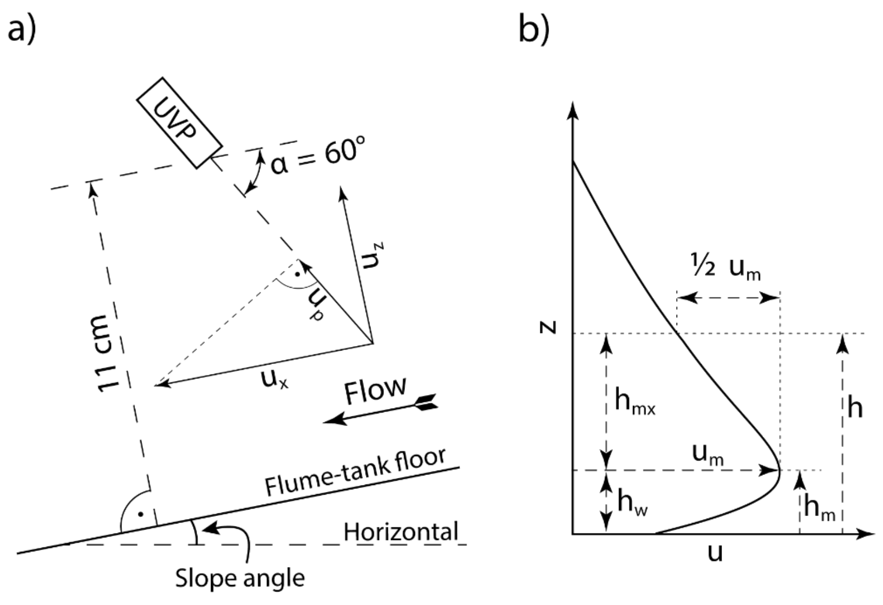

Fig. 2. (A) The orientation of the UVP. u_p: velocity measured by the probe. u_x: bed-parallel velocity component. u_z: bed-normal velocity component. (B) Sketch of a velocity

profile illustrating the parameterization. *z*: bed-normal coordinate. *u*: velocity. u_m: velocity maximum. *h*: flow thickness. h_m: elevation of the velocity maximum. h_w: thickness of the wall-region. h_{mx}: thickness of the mixing-region. Redrawn and modified after Launder & Rodi (1983). Not to scale.

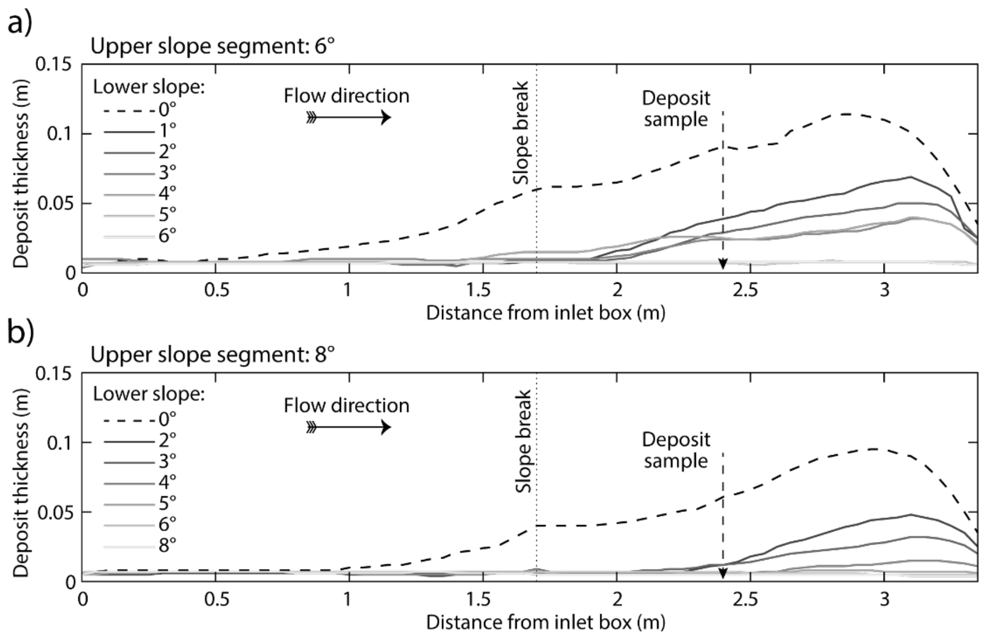

Fig. 3. Deposition profiles. (A) Experiments with an upper slope segment of 6°. (B) Experiments with an upper slope segment of 8°. Deposit thickness is increasing with a decreasing angle of the lower slope segment. The dashed line marks the experiments with a horizontal lower slope segment and a distinctly different deposition pattern due to a developing hydraulic jump. Also indicated the location at which deposit sample was taken. The decrease of the deposit thickness toward the end of the flume tank is caused by the transition into the expansion tank and an experimental artifact.

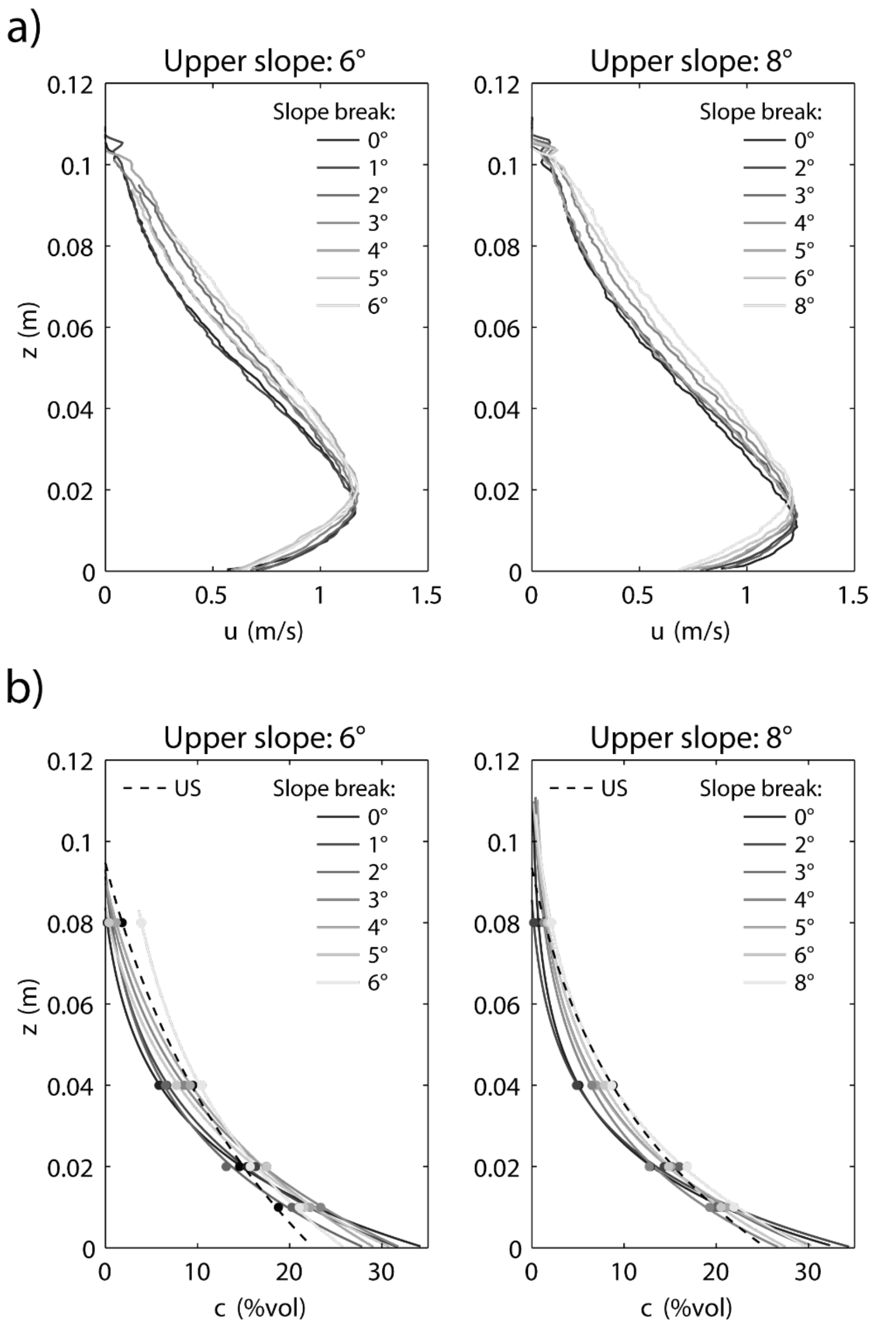

Fig. 4. (A) Time-averaged velocity profiles measured 0.6 m downstream of the slope break (i.e. 2.3 m downstream of the inlet box). (B) Sediment concentration profiles of the turbidity currents measured 0.8 m downstream of the slope break (i.e. 2.5 m downstream of the inlet box). The dashed line is a sediment concentration profile of the turbidity current that was sampled 0.3 m upstream of the slope break (i.e. 1.4 m downstream of the inlet box). US: upper slope segment.

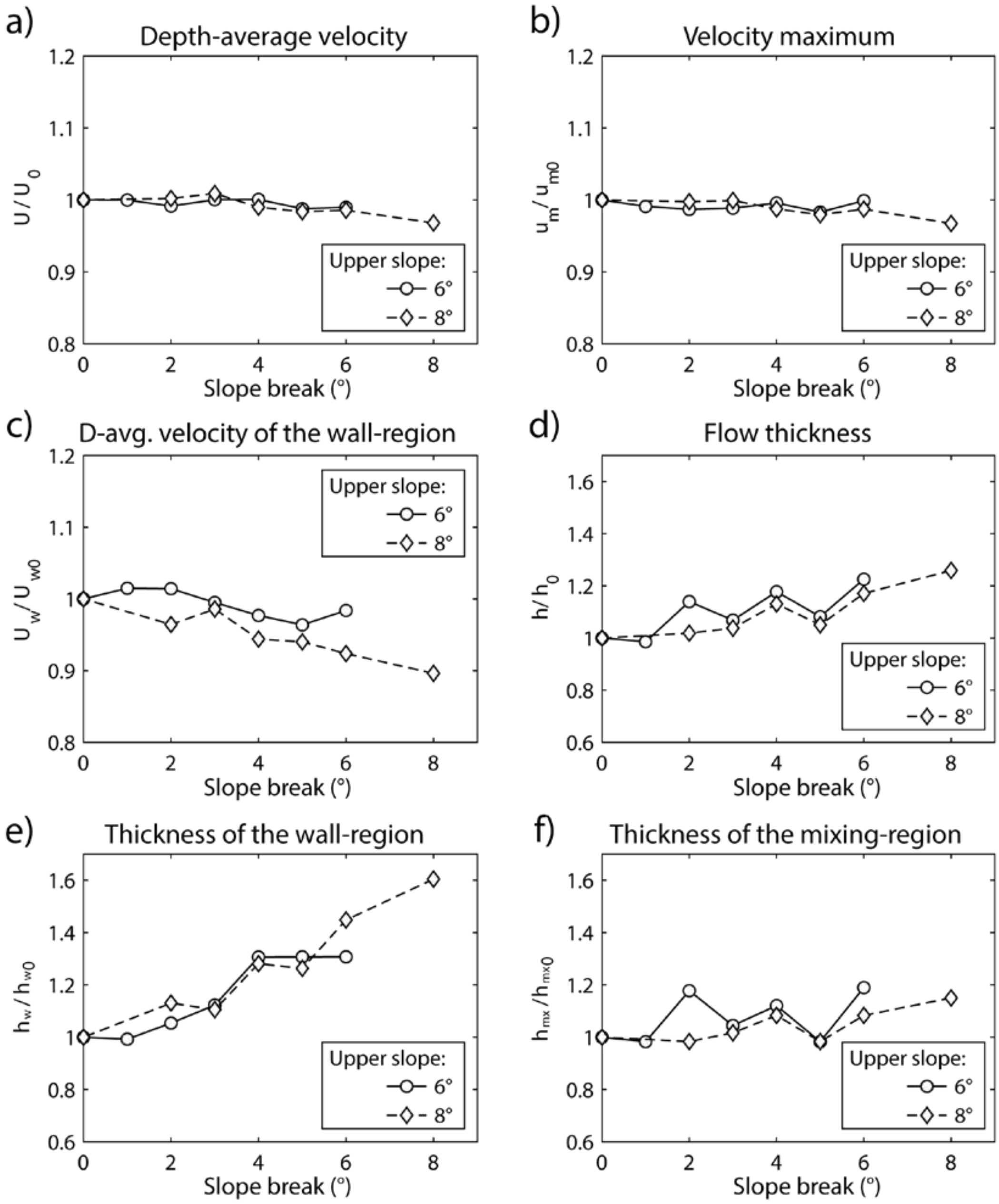

Fig. 5. Flow dimensions downstream of the slope break, normalized by the values measured in the 6° and 8° experiments without a slope break (Run 7 and 14 respectively). The absolute values can be found in Table 2. The depth-averaged velocity (A) and the velocity maximum (B) of the flow appears to be unaffected by the steepness of the slope-break angle. The velocity averaged over the depth of the wall region (C) is decreasing with an increasing steepness of the slope-break angle. The flow is thickening with an increasing slope-break

angle (D). Subdivision of the flow thickness into a wall-region (E) and a mixing-region (F) shows that the wall-region accounts for the majority of flow thickening.

		Velocity data						**Siphoning** (2.5m from the inlet box)						
								Height above the bed				Grain size at 1 cm		
Run	Slope break	U	u_m	U_w	h	w	m	8 cm	4 cm	2 cm	1 cm	d_{16}	d_{50}	d_{84}
	(°)	(m/s)	(m/s)	(m/s)	(m)	(m)	(m)		(%vol)				(µm)	
1	6	0.92	1.15	0.978	0.066	0.021	0.044	3.9	10.5	15.7	21.0	94.3	148.2	207.2
2	5	0.92	1.13	0.958	0.058	0.021	0.037	0.4	7.7	17.5	21.5	90.2	146.0	204.2
3	4	0.93	1.15	0.971	0.063	0.021	0.042	1.2	9.2	17.4	22.2	92.1	145.4	201.9
4	3	0.93	1.14	0.989	0.057	0.018	0.039	0.9	8.5	17.4	23.3	81.9	143.8	203.3
5	2	0.92	1.14	1.009	0.061	0.017	0.044	0.7	6.5	13.1	20.2	93.4	145.8	202.4
6	1	0.93	1.14	1.009	0.053	0.016	0.037	0.7	6.7	16.3	21.0	86.6	142.9	200.0
7	0	0.93	1.15	0.994	0.054	0.016	0.037	0.2	5.8	15.4	22.2	84.5	143.7	202.2
8	8	0.95	1.18	1.016	0.064	0.020	0.044	2.1	8.7	16.8	21.9	89.4	144.0	199.8
9	6	0.97	1.20	1.047	0.059	0.018	0.042	1.7	7.9	14.8	20.5	83.4	141.6	198.3
10	5	0.96	1.19	1.065	0.053	0.015	0.038	1.6	7.0	15.1	21.1	89.4	146.2	203.6
11	4	0.97	1.20	1.070	0.057	0.016	0.042	1.3	6.5	12.7	19.3	81.8	142.2	199.4
12	3	0.99	1.22	1.117	0.053	0.013	0.039	1.6	7.0	16.0	20.0	82.0	143.9	201.5
13	2	0.98	1.21	1.093	0.052	0.014	0.038	0.2	4.8	14.3	20.9	no data	no data	no data
14	0	0.98	1.22	1.133	0.051	0.012	0.038	0.7	5.1	12.8	21.0	83.4	141.8	198.5
							Upper slope	**Siphoning on the upper slope** (1.4 m from the inlet box)						
							6°	1.8	9.5	14.6	18.8	69.5	139.1	198.7
							8°	1.4	8.8	15.2	20.1	69.8	138.1	197.5

Table 2. Flow velocities and dimensions obtained from the time-averaged velocity profiles and the siphon tube samples.

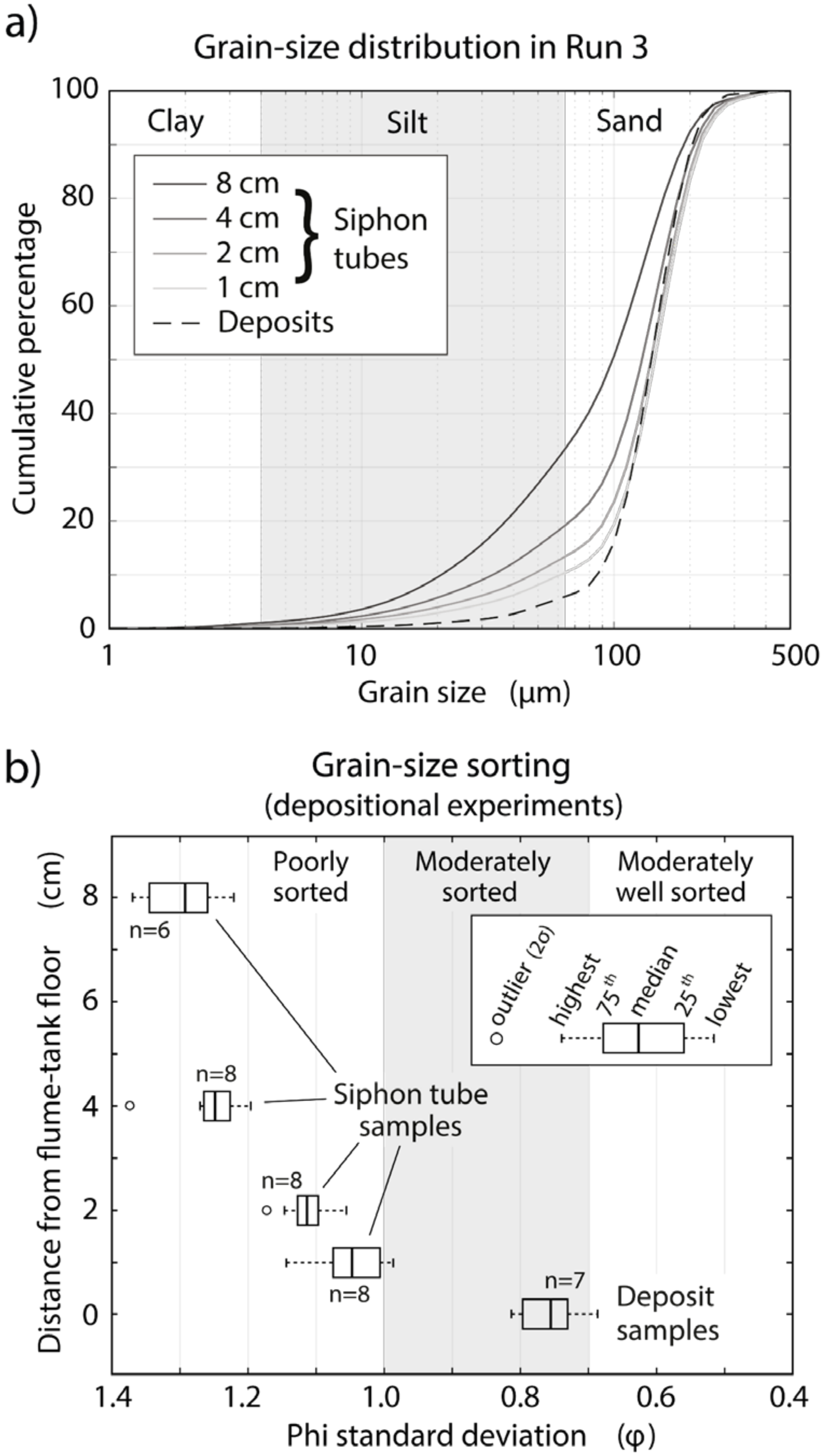
a)
Grain-size distribution in Run 3
Clay
Silt
Sand
8 cm
4 cm
2 cm
1 cm
Siphon tubes
Deposits
Cumulative percentage
100
80
60
40
20
0
1
10
100
500
Grain size (µm)
b)
Grain-size sorting
(depositional experiments)
Poorly sorted
Moderately sorted
Moderately well sorted
outlier (2σ)
highest
75th
median
25th
lowest
n=6
n=8
n=8
n=8
n=7
Siphon tube samples
Deposit samples
Distance from flume-tank floor (cm)
8
6
4
2
0
1.4
1.2
1.0
0.8
0.6
0.4
Phi standard deviation (φ)

687

Fig. 6. (A) Cumulative grain-size distribution of the sediment samples by siphoning and from the deposits. Shown here are the results of Run 3. The grain-size distribution curves of the remaining runs can be found in Figure S3. Coarsening of the grain size towards the flow base was mainly due to a decrease of the fine grain fraction in the distribution. The grain-size distribution of the deposits was coarser than that of the flow. (B) Box-and-whisker plots of the Phi standard deviation (sediment sorting) of the siphon samples and the deposits. Hollow circles mark outliers from the 2σ distribution. In the turbidity current, the sediment was better sorted towards the flow base. There appeared to be no correlation between the sediment sorting and the slope-break geometry. The deposits showed the lowest Phi standard deviation values and thus, were better sorted that the sediment suspended in the turbidity current.

Run	Aggr./ Non-Aggr.	Grain-size sorting				
		Deposits	Siphon tubes			
			8 cm	4 cm	2 cm	1 cm
		(ϕ)	(ϕ)	(ϕ)	(ϕ)	(ϕ)
1	A	0.781	1.269	1.236	1.057	1.009
2	A	0.812	no data	1.264	1.103	1.054
3	A	0.732	1.356	1.197	1.083	0.986
4	A	0.726	no data	1.375	1.173	1.144
5	A	0.756	1.258	1.232	1.111	1.002
6	N	–	–	–	–	–
7	N	–	–	–	–	–
8	A	0.687	1.318	1.212	1.114	1.039
9	A	0.811	1.222	1.261	1.121	1.068
10	A	no data	1.369	1.272	1.147	1.094
11	N	–	–	–	–	–
12	N	–	–	–	–	–
13	N	–	–	–	–	–
14	N	–	–	–	–	–

Table 3. Values of the Phi standard deviation (ϕ) of the siphon samples and the deposits that were plotted in Figure 6. The Phi standard deviation was calculated with the moment method. For some instances no grain-size data was obtained because insufficient sediment was collected at 8 cm above the bed (Runs 2, 4, and 10). Siphon-samples for non-aggrading runs were not analysed for grainsize because comparison with the bed was not possible and grain size stratification did not vary between runs in the available dataset.

Run	Slope break	Flow parameters			
		u_*	Fr'	Γ	Aggr./ Non-Aggr.
	(°)	(m/s)	(-)	(-)	
1	6	0.067	2.54	0.62	A
2	5	0.065	2.66	0.57	A
3	4	0.066	2.59	0.58	A
4	3	0.067	2.62	0.58	A
5	2	0.068	2.87	0.68	A
6	1	0.069	2.80	0.68	N
7	0	0.069	2.82	0.66	N
8	8	0.069	2.67	0.66	A
9	6	0.071	2.89	0.78	A
10	5	0.072	2.93	0.79	A
11	4	0.073	3.09	0.88	N
12	3	0.075	3.02	0.94	N
13	2	0.075	3.11	0.89	N
14	0	0.076	3.16	0.94	N

Table 4. Calculated flow parameters that were plotted in Figures 7 and 8.

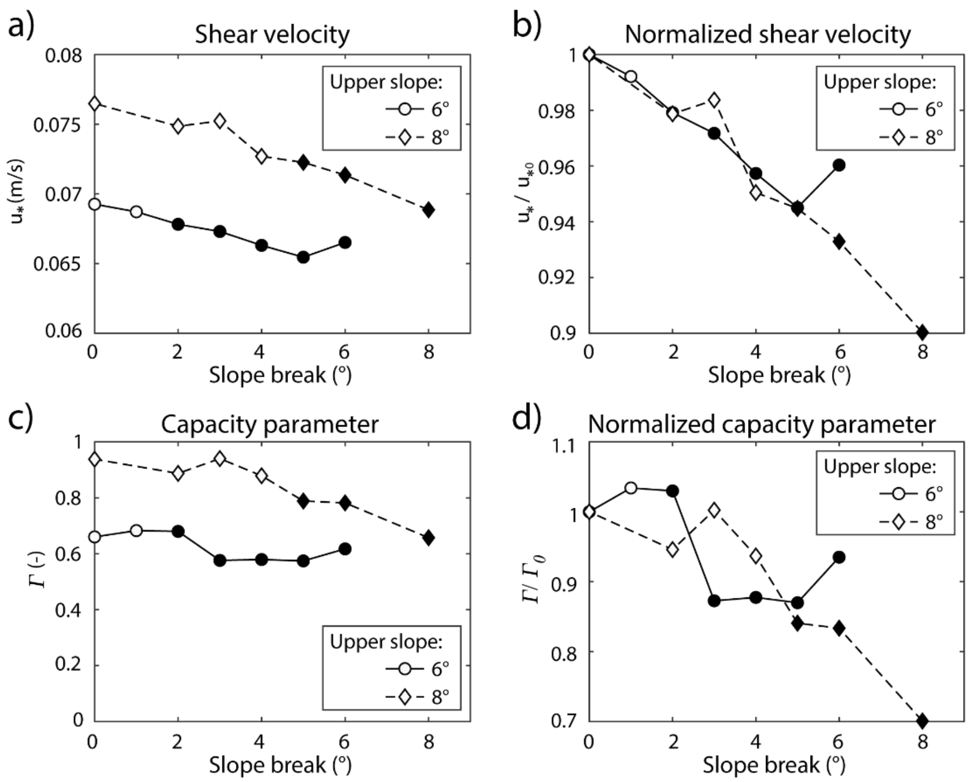

Fig. 7. (A) Absolute values of the shear velocity against the slope-break angle. The solid black markers indicate experiments with depositional turbidity currents and the hollow markers currents with bypassing flows. (B) Shear velocity normalized by the values measured in the 6° and 8° experiments without a slope break. Shear velocities are decreasing with an increasing steepness of the slope-break angle. (C) Absolute values of the capacity criterion against the slope-break angle. (D) Capacity parameter normalized by the values measured in the 6° and 8° experiments without a slope break. The capacity of the flow is decreasing with an increasing slope-break angle.

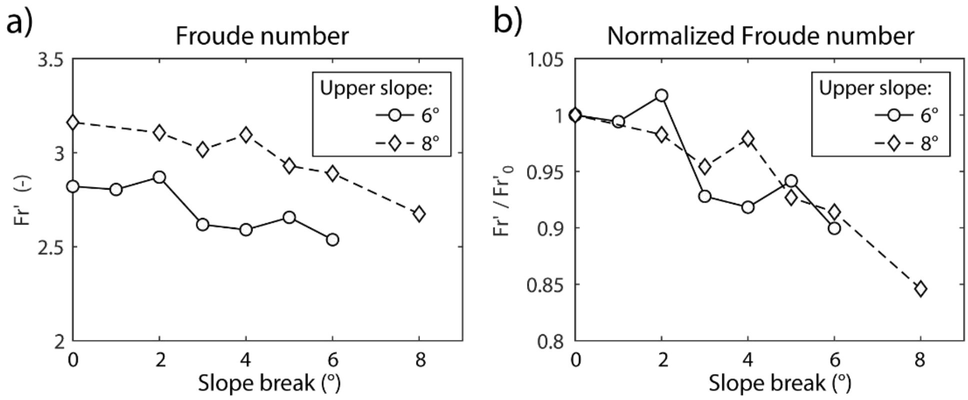

Fig. 8. (A) Absolute values of the densiometric Froude number (depth-averaged) against the slope-break angle. (B) Froude number normalized by the Froude number value obtained from the 6° and 8° experiments without a slope break. Densiometric Froude number was decreasing with an increasing slope-break angle. However, values remained above unity and flows supercritical.

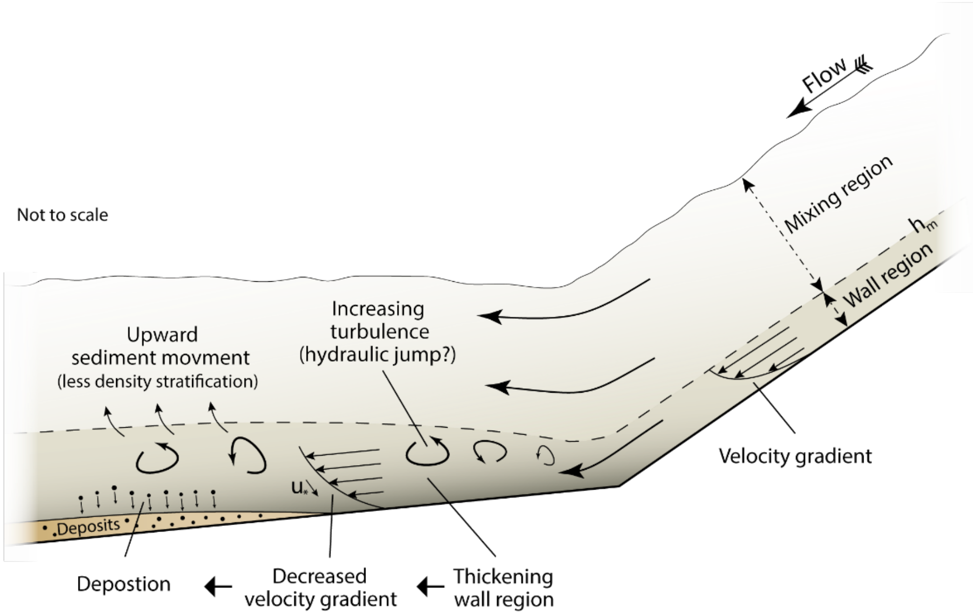

Fig. 9. Flow-dynamic model for a turbidity current crossing a slope break. Elevation of the velocity maximum (h_m) results in thickening of the wall-region (h_w) and decrease of the shear velocity (u_*). Reduced shear velocity results in deposition. Turbulence production, at and due to the slope break, causes an upward sediment movement reflected by a decreased density stratification downstream of the slope break.

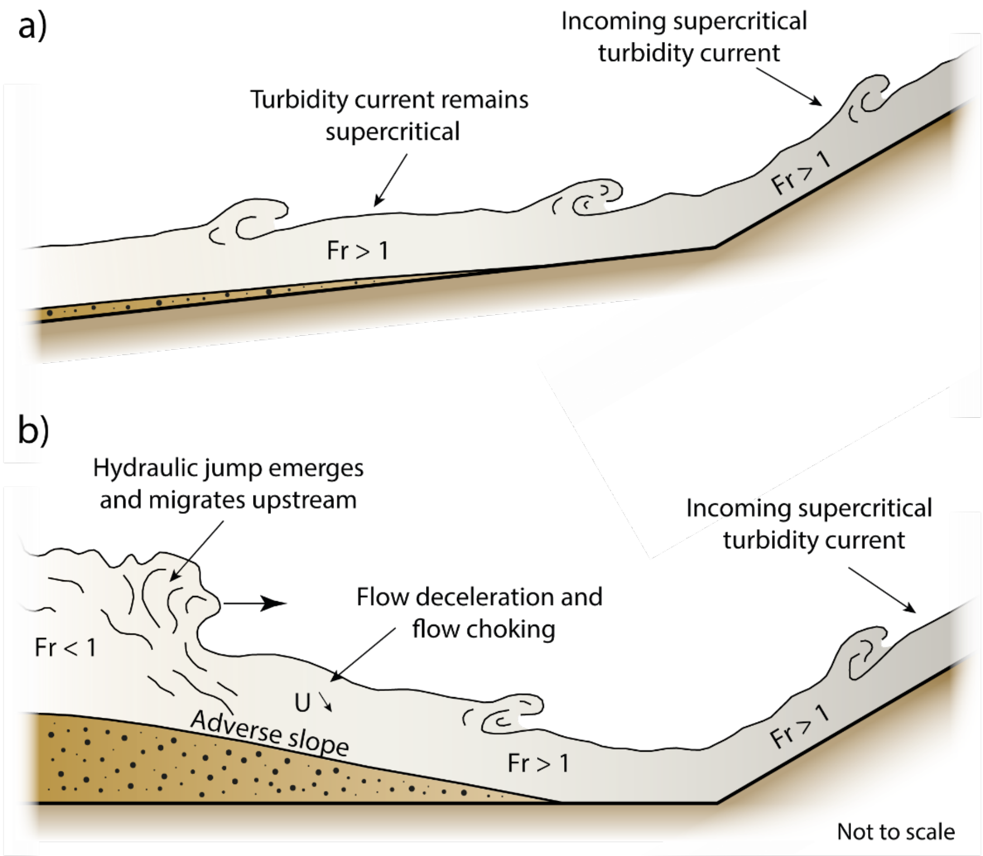

Fig. 10. (A) Supercritical turbidity current crossing a slope break and depositing sediment in the absence of a hydraulic jump. (B) The incoming same turbidity current but deposition on the lower slope segment formed a ramp with an adverse slope. The flow decelerates, chokes, and a hydraulic jump emerges that migrates upstream. Fr: Froude number, U: Depth-averaged velocity.

REFERENCES

Altinakar, M.S., **Graf, W.H.** and **Hopfinger, E.J.** (1996) Flow structure in turbidity currents. *J. Hydraul. Res.*, **34**, 713–718.

Azpiroz-Zabala, M., **Cartigny, M.J.B.**, **Talling, P.J.**, **Parsons, D.R.**, **Sumner, E.J.**, **Clare, M.A.**, **Simmons, S.M.**, **Cooper, C.** and **Pope, E.L.** (2017) Newly recognized turbidity current structure can explain prolonged flushing of submarine canyons. *Sci. Adv.*, **3**, 1–12.

Baas, J.H., **van Kesteren, W.** and **Postma, G.** (2004) Deposits of depletive high-density turbidity currents: A flume analogue of bed geometry, structure and texture. *Sedimentology*, **51**, 1053–1088.

Boggs, S.J. (2009) Petrology of Sedimentary Rocks. In: *Petrology of Sedimentary Rocks* (Ed. J.S. Boggs), *Cambridge University Press, 21-49*, Cambridge,

Bonnel, C., **Dennielou, B.**, **Droz, L.**, **Mulder, T.** and **Berné, S.** (2005) Architecture and depositional pattern of the Rhône Neofan and recent gravity activity in the Gulf of Lions (western Mediterranean). *Mar. Pet. Geol.*, **22**, 827–843.

Bouma, A.H., **Normark, W.R.** and **Barnes, N.E.** (2012) Submarine Fans and Related Turbidite Systems. *Springer. 351 pp.*, New York, 351 pp.

Bourget, J., **Zaragosi, S.**, **Ellouz-Zimmermann, N.**, **Mouchot, N.**, **Garlan, T.**, **Schneider, J.L.**, **Lanfumey, V.** and **Lallemant, S.** (2011) Turbidite system architecture and sedimentary processes along topographically complex slopes: The Makran convergent margin. *Sedimentology*, **58**, 376–406.

Brooks, H.L., **Hodgson, D.M.**, **Brunt, R.L.**, **Peakall, J.**, **Hofstra, M.** and **Flint, S.S.** (2018) Deep-water channel-lobe transition zone dynamics: Processes and depositional architecture, an example from the Karoo Basin, South Africa. *GSA Bull.*, **130**, 1723–1746.

Buckee, C., **Kneller, C.** and **Peakall, J.** (2001) Turbulence structure in steady, solute-driven gravity currents. In: *Particulate gravity currents* (Ed. W.D. Mccaffrey, B. Kneller, and J. Peakall), *International Association of Sedimentologists, Special Publication 31, Blackwell Science*, 173–188.

Cantero, M.I., **Balachandar, S.**, **Cantelli, A.** and **Parker, G.** (2014) A simplified approach to address turbulence modulation in turbidity currents as a response to slope breaks and loss of lateral confinement. *Environ. Fluid Mech.*, **14**, 371–385.

Cartigny, M.J.B., **Eggenhuisen, J.T.**, **Hansen, E.W.M.** and **Postma, G.** (2013) Concentration-Dependent Flow Stratification In Experimental High-Density Turbidity Currents and Their Relevance To Turbidite Facies Models. *J. Sediment. Res.*, **83**, 1046–1064.

Chanson, H. (2004) Hydraulics of open channel flow. *Elsevier. 650 pp.*, 650 pp.

Choi, S.-U. and **Garcia, M.H.** (1995) Modeling of one-dimensional turbidity currents with a dissipative-Galerkin finite element method. *J. Hydraul. Res.*, **33**, 623–648.

de Leeuw, J., **Eggenhuisen, J.T.** and **Cartigny, M.J.B.** (2016) Morphodynamics of submarine channel inception revealed by new experimental approach. *Nat. Commun.*, **7**, 1–7.

de Leeuw, J., **Eggenhuisen, J.T.** and **Cartigny, M.J.B.** (2018a) Linking submarine channel–levee facies and architecture to flow structure of turbidity currents: insights from flume tank experiments. *Sedimentology*, **65**, 931–951.

de Leeuw, J., **Eggenhuisen, J.T.**, **Spychala, Y.T.**, **Heijnen, M.S.**, **Pohl, F.** and **Cartigny, M.J.B.** (2018b) Sediment Volume and Grain-Size Partitioning Between Submarine Channel−Levee Systems and Lobes: An Experimental Study. *J. Sediment. Res.*, **88**, 777–794.

Dorrell, R.M., **Hogg, A.J.** and **Pritchard, D.** (2013) Polydisperse suspensions: Erosion, deposition, and flow capacity. *J. Geophys. Res. Earth Surf.*, **118**, 1939–1955.

Dorrell, R.M., **Peakall, J.**, **Sumner, E.J.**, **Parsons, D.R.**, **Darby, S.E.**, **Wynn, R.B.**, **Özsoy, E.** and **Tezcan, D.** (2016) Flow dynamics and mixing processes in hydraulic jump arrays: Implications for channel-lobe transition zones. *Mar. Geol.*, **381**, 181–193.

Eggenhuisen, J.T., **Cartigny, M.J.B.** and **de Leeuw, J.** (2017) Physical theory for near-bed turbulent particle suspension capacity. *Earth Surf. Dyn.*, **5**, 269–281.

Eggenhuisen, J.T. and **McCaffrey, W.D.** (2012) The vertical turbulence structure of experimental turbidity currents encountering basal obstructions: Implications for vertical suspended sediment distribution in non-equilibrium currents. *Sedimentology*, **59**, 1101–1120.

Fernandes, A.M., **Buttles, J.** and **Mohrig, D.** (2020) Flow substrate interactions in aggrading and degrading submarine channels. *J. Sediment. Res.*, **90**, 573–583.

Galy, V., **France-Lanord, C.**, **Beyssac, O.**, **Faure, P.**, **Kudrass, H.** and **Palhol, F.** (2007) Efficient organic carbon burial in the Bengal fan sustained by the Himalayan erosional system. *Nature*, **450**, 407–410.

Garcia, M. and **Parker, G.** (1989) Experiments on hydraulic jumps in turbidity currents near a canyon-fan transition. *Science (80-.).*, **245**, 393–396.

Garcia, M.H. (1993) Hydraulic Jumps in Sediment-Driven Bottom Currents. *J. Hydraul. Eng.*, **119**, 1094–1117.

Garcia, M.H. (1994) Depositional Turbidity Currents Laden with Poorly Sorted Sediment. *J. Hydraul. Eng.*, **120**, 1240–1263.

Gray, T.E., **Alexander, J.** and **Leeder, M.R.** (2006) Longitudinal flow evolution and turbulence structure of dynamically similar, sustained, saline density and turbidity currents. *J. Geophys. Res. Ocean.*, **111**, 1–14.

Gray, T.E., **Alexander, J.** and **Leeder, M.R.** (2005) Quantifying velocity and turbulence structure in depositing sustained turbidity currents across breaks in slope. *Sedimentology*, **52**, 467–488.

Habgood, E.L., **Kenyon, N.H.**, **Masson, D.G.**, **Akhmetzhanov, A.**, **Weaver, P.P.E.**, **Gardner, J.** and **Mulder, T.** (2003) Deep-water sediment wave fields, bottom current sand channels and gravity flow channel-lobe systems: Gulf of Cadiz, NE Atlantic. *Sedimentology*, **50**, 483–510.

Hage, S., **Galy, V. V.**, **Cartigny, M.J.B.**, **Acikalin, S.**, **Clare, M.A.**, **Gröcke, D.R.**, **Hilton, R.G.**, **Hunt, J.E.**, **Lintern, D.G.**, **Mcghee, C.A.**, **Parsons, D.R.**, **Stacey, C.D.**, **Sumner, E.J.** and **Talling, P.J.** (2020) Efficient preservation of young terrestrial organic carbon in sandy turbidity-current deposits. *Geology*, **48**, 882–887.

Hamilton, P., **Gaillot, G.**, **Strom, K.**, **Fedele, J.** and **Hoyal, D.** (2017) Linking hydraulic properties in supercritical submarine distributary channels to depositional-lobe geometry. *J. Sediment. Res.*, **87**, 935–950.

Hamilton, P.B., **Strom, K.B.** and **Hoyal, D.C.J.D.** (2015) Hydraulic and sediment transport properties of autogenic avulsion cycles on submarine fans with supercritical distributaries. *J. Geophys. Res. F Earth Surf.*, **120**, 1369–1389.

Hein, J.R., **Mizell, K.**, **Koschinsky, A.** and **Conrad, T.A.** (2013) Deep-ocean mineral deposits as a source of critical metals for high- and green-technology applications: Comparison with land-based resources. *Ore Geol. Rev.*, **51**, 1–14.

Hiscott, R.N. (1994) Loss of capacity, not competence, as the furndamental process governing deposition from turbidity currents. *J. Sediment. Res.*, **A64**, 209–214.

Hofstra, M., **Hodgson, D.M.**, **Peakall, J.** and **Flint, S.S.** (2015) Giant scour-fills in ancient channel-lobe transition zones: Formative processes and depositional architecture. *Sediment. Geol.*, **329**, 98–114.

Hoyal, D.C.J.D. and **Sheets, B.A.** (2009) Morphodynamic evolution of experimental cohesive deltas. *J. Geophys. Res. Earth Surf.*, **114**, 1–18.

Huang, H., **Imran, J.**, **Pirmez, C.**, **Zhang, Q.** and **Chen, G.** (2009) The Critical Densimetric Froude Number of Subaqueous Gravity Currents Can Be Non-Unity or Non-Existent. *J. Sediment. Res.*, **79**, 479–485.

Islam, M.A. and **Imran, J.** (2010) Vertical structure of continuous release saline and turbidity currents. *J. Geophys. Res. Ocean.*, **115**, 1–14.

Ito, M., **Ishikawa, K.** and **Nishida, N.** (2014) Distinctive erosional and depositional structures formed at a canyon mouth: A lower Pleistocene deep-water succession in the Kazusa forearc basin on the Boso Peninsula, Japan. *Sedimentology*, **61**, 2042–2062.

Kato, Y., **Fujinaga, K.**, **Nakamura, K.**, **Takaya, Y.**, **Kitamura, K.**, **Ohta, J.**, **Toda, R.**, **Nakashima, T.** and **Iwamori, H.** (2011) Deep-sea mud in the Pacific Ocean as a potential resource for rare-earth elements. *Nat. Geosci.*, **4**, 535–539.

Kenyon, N.H. and **Millington, J.** (1995) Contrasting deep-sea depositional systems in the Bering Sea. In: *Atlas of Deep Water Environments* (Ed. K.T. Pickering, R.N. Hiscott, N.H. Kenyon, F. Ricci Lucchi, and R.D.A. Smith), *Springer Netherlands*, Dordrecht, 196–202.

Kneller, B. (2003) The influence of flow parameters on turbidite slope channel architecture. *Mar. Pet. Geol.*, **20**, 901–910.

Kneller, B. and **Buckee, C.** (2000) The structure and fluid mechanics of turbidity currents: a review of some recent studies and their geological implications. *Sedimentology*, **47**, 62–94.

Kneller, C., **Bennett, S.J.** and **Mccaffrey, W.D.** (1999) Velocity structure, turbulence and fluid stresses in experimnetal gravity currents. *J. Geophys. Res.*, **104**, 5381–5391.

Komar, P.D. (1971) Hydraulic jumps in turbidity currents. *Bull. Geol. Soc. Am.*, **82**, 1477–1488.

Kostic, S. and **Parker, G.** (2006) The response of turbidity currents to a canyon-fan transition: Internal hydraulic jumps and depositional signatures. *J. Hydraul. Res.*, **44**, 631–653.

Kostic, S. and **Parker, G.** (2007) Conditions under which a supercritical turbidity current traverses an abrupt transition to vanishing bed slope without a hydraulic jump. *J. Fluid Mech.*, **586**, 119–145.

Kuenen, P.H. and **Sengupta, S.** (1970) Experimental marine suspension currents, competency and capacity. *Geol. en Mijnb.*, **49**, 89–118.

Launder, B.E. and **Rodi, W.** (1983) The Turbulent Wall Jet Measurements and Modeling. *Annu. Rev. Fluid Mech.*, **15**, 429–459.

Lee, S.E., **Talling, P.J.**, **Ernst, G.G.J.** and **Hogg, A.J.** (2002) Occurrence and origin of submarine plunge pools at the base of the US continental slope. *Mar. Geol.*, **185**, 363–377.

Lemmin, U. and **Rolland, T.** (1997) Acoustic Velocity Profiler for Laboratory and Field Studies. *J. Hydraul. Eng.*, **123**, 1089–1098.

Long, D., **Rajaratnam, N.**, **Steffler, P.M.** and **Smy, P.R.** (1991) Structure of flow in hydraulic jumps. *J. Hydraul. Res.*, **29**, 207–218.

Macdonald, H.A., **Wynn, R.B.**, **Huvenne, V.A.I.**, **Peakall, J.**, **Masson, D.G.**, **Weaver, P.P.E.** and **McPhail, S.D.** (2011) New insights into the morphology, fill, and remarkable longevity (>0.2 m.y.) of modern deep-water erosional scours along the northeast Atlantic margin. *Geosphere*, **7**, 845–867.

Marr, J.G., **Shanmugam, G.** and **Parker, G.** (2001) Experiments on subaqueous sandy gravity flows: The role of clay and water content in flow dynamics and depositional structures. *Bull. Geol. Soc. Am.*, **113**, 1377–1386.

Middleton, G. V and **Southard, J.B.** (1984) Mechanics of Sediment Movement. *SEPM, Eastern Section Short Course 3 Providence, 401 pp.*

Morris, S.A., **Kenyon, N.H.**, **Limonov, A.F.** and **Alexander, J.** (1998) Downstream changes of large-scale bed forms in turbidites around the Valencia channel mouth, north-west Mediterranean: Implications for palaeoflow reconstruction. *Sedimentology*, **45**, 365–377.

Mulder, T. and **Alexander, J.** (2001) Abrupt change in slope causes variation in the deposit thickness of concentrated particle-driven density currents. *Mar. Geol.*, **175**, 221–235.

Mutti, E., **Bernoulli, D.**, **Lucchi, F.R.** and **Tinterri, R.** (2009) Turbidites and turbidity currents from alpine “flysch” to the exploration of continental margins. *Sedimentology*, **56**, 267–318.

Mutti, E. and **Normark, W.R.** (1987) Comparing Examples of Modern and Ancient Turbidite Systems: Problems and Concepts. In: *Marine Clastic Sedimentology* (Ed. J.K. Leggett and G.G. Zuffa), *Springer*, Dordrecht, 1–38.

Nelson, C.H., **Goldfinger, C.**, **Johnson, J.E.** and **Dunhill, G.** (2000) Variation of modern turbidite systems along the subduction zone margin of Cascadia Basin and implications for turbidite reservoir beds. In: *DeepWater Reservoirs of the World* (Ed. P.W. Weimer and C.H. Nelson), *20th Annual Research Conference, Gulf Coast Section Society of Economic Paleontologists and Mineralogists*, 714–738.

Nilsen, T.H., **Shew, R.D.**, **Steffens, G.S.** and **Studlick, J.R.J.** (2008) Studlick, Atlas of Deep-Water Outcrops.

AAPG Studies in Geology 56 & Shell Exploration & Production. 504 pp.

Normark, W.R. (1970) Growth patterns of deep-sea fans. *Am. Assoc. Pet. Geol. Bull.*, **54**, 2170–2195.

Palanques, A., **Kenyon, N.H.**, **Alonso, B.** and **Limonov, A.** (1996) Erosional and depositional patterns in the Valencia Channel mouth: An example of a modern channel-lobe transition zone. *Mar. Geophys. Res.*, **18**, 104–118.

Pettingill, H.S. (2004) Global Overview of Deepwater Exploration and Production. In: *Petroleum Systems of Deepwater Settings* (Ed. P. Weimer, H.S. Pettingill, and T.H. Nilsen), *Society of Exploration Geophysicists and European Association of Geoscientists and Engineers*, 57, 1–40.

Piper, D.J.W. and **Savoye, B.** (1993) Processes of Late Quaternary turbidity-current flow and deposition on the Var deep-sea fan, North-west Mediterranean Sea. *Sedimentology*, **40**, 557–582.

Pohl, F., **Eggenhuisen, J.T.**, **Cartigny, M.J.B.**, **Tilston, M.C.**, **de Leeuw, J.** and **Hermidas, N.** (2020a) The influence of a slope break on turbidite deposits: An experimental investigation. *Mar. Geol.*, **424**, 106160.

Pohl, F., **Eggenhuisen, J.T.**, **Kane, I.A.** and **Clare, M.A.** (2020b) Transport and Burial of Microplastics in Deep-Marine Sediments by Turbidity Currents. *Environ. Sci. Technol.*, **54**, 4180–4189.

Pohl, F., **Eggenhuisen, J.T.**, **Tilston, M.** and **Cartigny, M.J.B.** (2019) New flow relaxation mechanism explains scour fields at the end of submarine channels. *Nat. Commun.*, **10**, 4425.

Postma, G. and **Kleverlaan, K.** (2018) Supercritical fl ows and their control on the architecture and facies of small-radius sand-rich fan lobes. *Sediment. Geol.*, **364**, 53–70.

Rajaratnam, N. (1967) Hydraulic Jumps. *Adv. Hydrosci.*, **4**, 197–280.

Rouse, H. (1937) Modern conceptions of the mechanics of fluid turbulence. *Am. Soc. Civ. Eng. Trans.*, **102**, 463–543.

Salinas, J., **Balachandar, S.**, **Shringarpure, M.**, **Fedele, J.**, **Hoyal, D.** and **Cantero, M.** (2020) Soft transition between subcritical and supercritical currents through intermittent cascading interfacial instabilities. *Proc. Natl. Acad. Sci.*, **117**, 18278–18284.

Sequeiros, O.E., **Mosquera, R.** and **Pedocchi, F.** (2018) Internal Structure of a Self-Accelerating Turbidity Current. *J. Geophys. Res. Ocean.*, **123**, 6260–6276.

Shields, A. (1936) Anwendung der Aehnlichkeitsmechanig und der Turbulenzforschung auf die Geschiebebewegung. Technische Hochschule Berlin, 25 pp

Spychala, Y.T., **Eggenhuisen, J.T.**, **Tilston, M.** and **Pohl, F.** (2020) The influence of basin setting and turbidity current properties on the dimensions of submarine lobe elements. Sedimentology. doi: 10.1111/sed.12751

Steel, E., **Buttles, J.**, **Simms, A.R.**, **Mohrig, D.** and **Meiburg, E.** (2017) The role of buoyancy reversal in turbidite deposition and submarine fan geometry. *Geology*, **45**, 35–38.

Stevenson, C.J., **Jackson, C.A.-L.**, **Hodgson, D.M.**, **Hubbard, S.M.** and **Eggenhuisen, J.T.** (2015) Deep-Water Sediment Bypass. *J. Sediment. Res.*, **85**, 1058–1081.

Takeda, Y. (1995) Velocity profile measurement by ultrasonic Doppler method. *Exp. Therm. Fluid Sci.*, **10**, 444–453.

Talling, P.J., **Allin, J.**, **Armitage, D. a**, **Arnott, R.W.**, **Cartigny, M.J.**, **Clare, M. a**, **Felletti, F.**, **Covault, J. a**, **Girardclos, S.**, **Hansen, E.**, **Hill, P.R.**, **Hiscott, R.N.**, **Hogg, A.J.**, **Hughes Clarke, J.**, **Jobe, Z.R.**, **Malgesini, G.** and **Mozzato, A.** (2015) Key Future Directions for Research on Turbidity Currents and Their Deposits. *J. Sediment. Res.*, **85**, 153–169.

Talling, P.J., **Wynn, R.B.**, **Masson, D.G.**, **Frenz, M.**, **Cronin, B.T.**, **Schiebel, R.**, **Akhmetzhanov, A.M.**, **Dallmeier-Tiessen, S.**, **Benetti, S.**, **Weaver, P.P.E.**, **Georgiopoulou, A.**, **Zühlsdorff, C.** and **Amy, L.A.** (2007) Onset of submarine debris flow deposition far from original giant landslide. *Nature*, **450**, 541–544.

Toniolo, H., **Parker, G.**, **Voller, V.** and **Beaubouef, R.T.** (2006) Depositional Turbidity Currents in Diapiric Minibasins on the Continental Slope: Experiments–Numerical Simulation and Upscaling. *J. Sediment. Res.*, **76**, 798–818.

van Rijn, L.C. (1993) Principles of sediment transport in rivers, estuaries and coastal seas. *Aqua publications. 790 pp.*, Amsterdam, 790 pp.

Vellinga, A.J., **Cartigny, M.J.B.**, **Eggenhuisen, J.T.** and **Hansen, E.W.M.** (2018) Morphodynamics and depositional signature of low-aggradation cyclic steps: New insights from a depth-resolved numerical model. *Sedimentology*, **65**, 540–560.

Weirich, F.H. (1988) Field evidence for hydraulic jumps in subaqueous sediment gravity flows. *Nature*, **332**, 626–629.

Wood, I.R. (1967) Horizontal Two-Dimensional Density Current. *J. Hydraul. Div.*, **93**, 35–42.

Wynn, R.B., **Kenyon, N.H.**, **Masson, D.G.**, **Stow, D.A.V.** and **Weaver, P.P.E.** (2002) Characterization and recognition of deep-water channel-lobe transition zones. *Am. Assoc. Pet. Geol. Bull.*, **86**, 1441–1462.

Supplementary material for:

Initiation of deposition in supercritical turbidity currents downstream of a slope break

Pohl, F.[a]*, Eggenhuisen, J.T.[b], Cartigny, M.J.B.[c], Tilston, M.[d]

[e] Marine School of Biological and Marine Sciences, University of Plymouth, Drake Circus, PL4 8AA Plymouth, UK

[f] Faculty of Geosciences, Utrecht University, P.O. box 80021, 3508 TA Utrecht, The Netherlands

[g] Department of Geography, Durham University, Lower Mountjoy South Road, DH1 3LE Durham, UK

[h] Department of Geosciences, University of Calgary, 2500 University Dr. T2N 1N4 Calgary, Alberta, Canada

* Corresponding author: florian.pohl@plymouth.ac.uk

Contents of this file

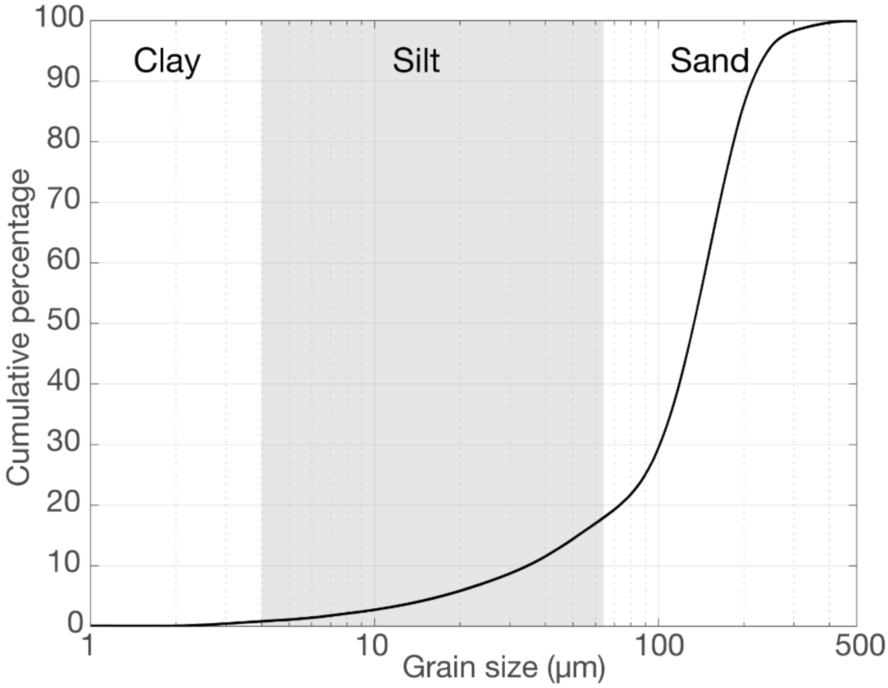

Fig. S1. Grain-size distribution of the sediment used for the turbidity current and glued to the flume tank floor. The grain-size distribution was measured with a laser particle sizer (Malvern Mastersizer 2000).

Manufacturer and type	MET-FLOW; DUO MX
Speed of sound in water (m/s)	1480
Measurement window (mm)	175.38
Number of channels	238
Distance between channel centers (mm)	0.74
Channel width (mm)	3.7
Frequency of the ultrasound beam (MHz)	1
Number of cycles per pulse	5
Number of sound pulses per measurement	32
Minimum on-axis velocity (mm/s)	-1516.4
Maximum on-axis velocity (mm/s)	1504.5
On-axis velocity resolution (mm/s)	11.8
Pulse repetition frequency (kHz)	4.1

Table S1. UVP data acquisition settings.

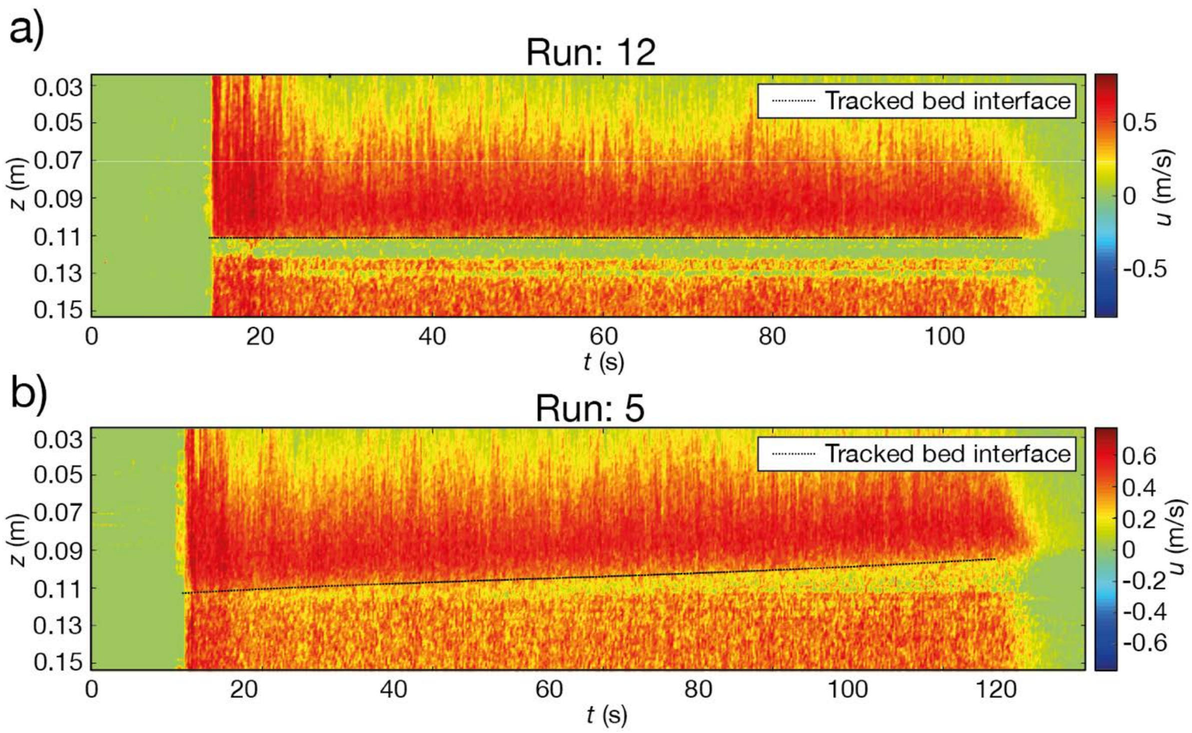

Fig. S2. Turbidity current velocity over time as measured by the UVP for two experiments. Indicated with a dotted line is the tracked bed interface between the bed and the turbidity current, marked by a high vertical-velocity-gradient. (A) Measurements of run 12 with no sediment accreting underneath the UVP. (B) Measurements of run 5, where sediment was accreting underneath the UVP, resulting in a decreasing distance from the bed to the UVP. The velocity signal below the tracked bed interface (i.e. > 0.13 m away from the probe) is an interference pattern and an artifact of the measurement.

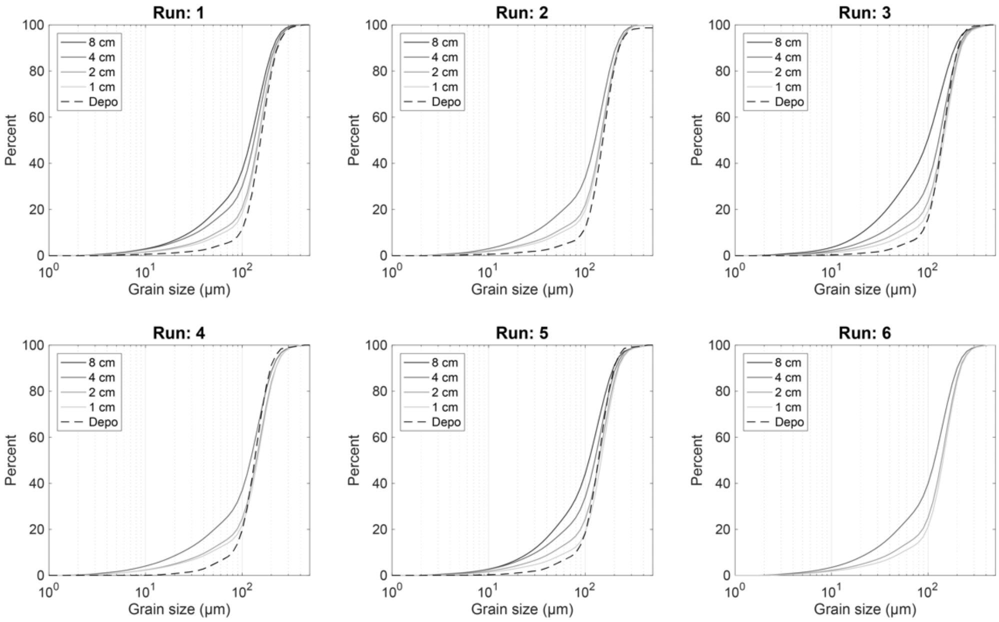

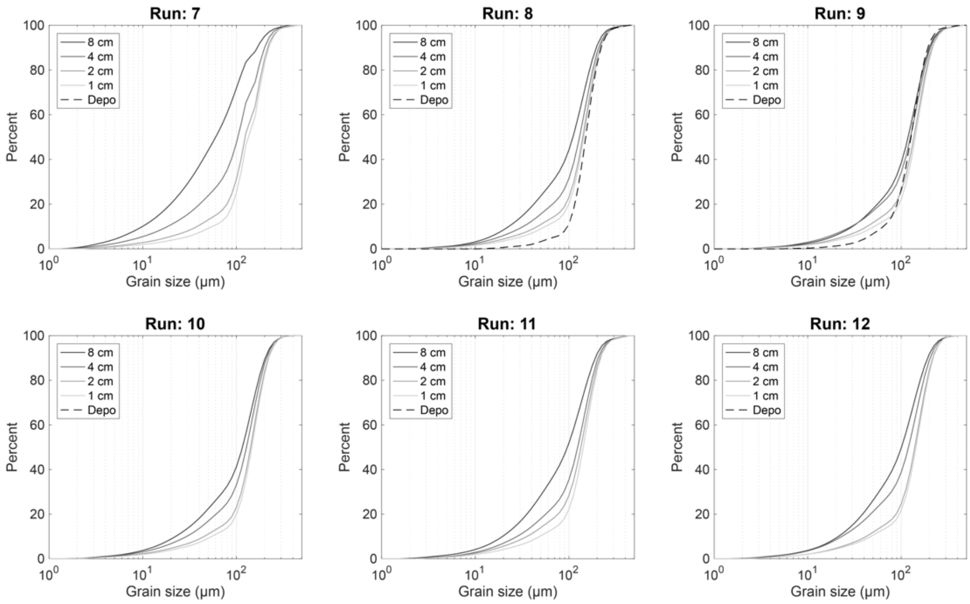

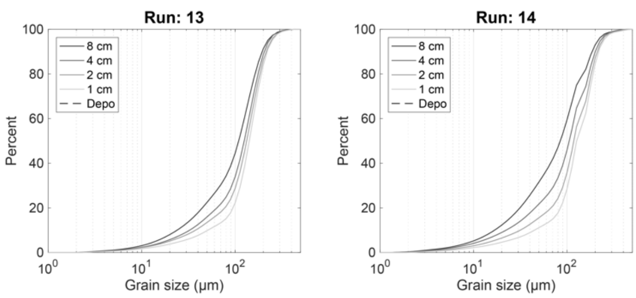

Fig. S3. Cumulative grain-size distributions from the siphon samples and the deposits.

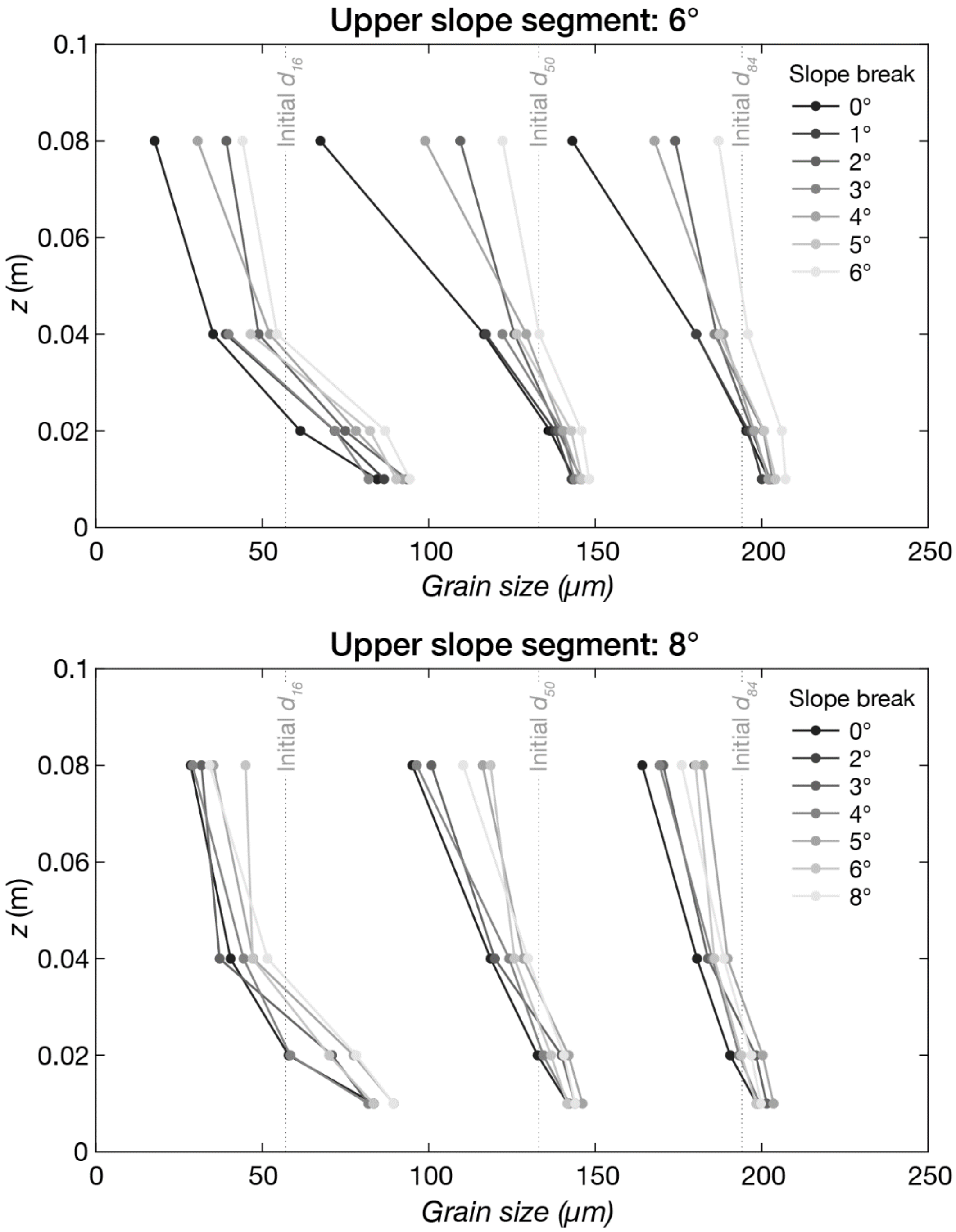

Fig. S4. Grain-size distributions measurements from the siphon samples. Shown from left to right are the d_{16}, the d_{50}, and the d_{84}. The solid lines mark the samples of the siphon tubes on the lower slope, 2.5 m downstream of the inlet box. The dotted gray line indicates the grain size of the initial mixture.

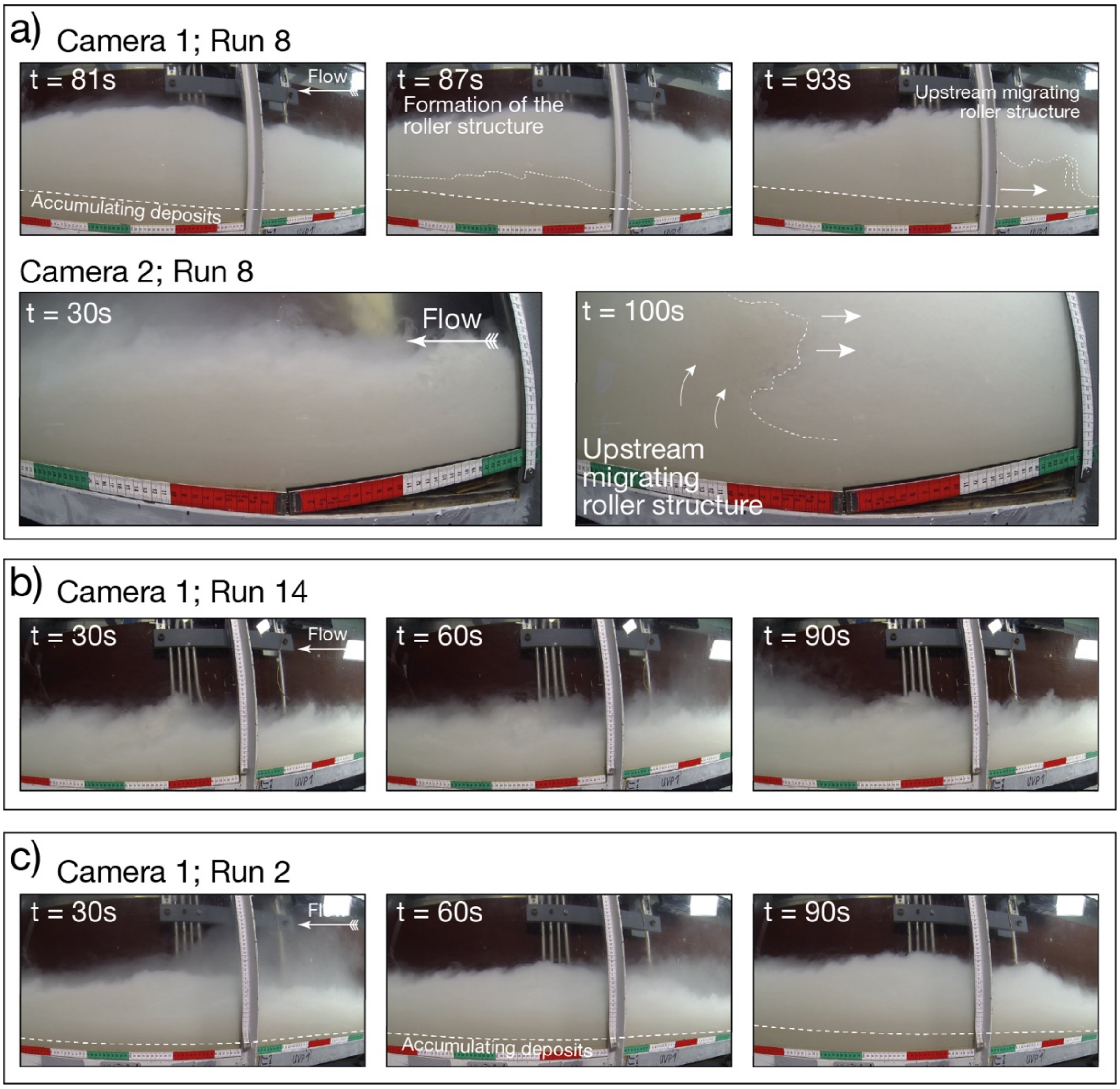

Fig. S5. Snapshots of videos of the flow through the flume-tank side wall; see Figure 1 for field of view. The green, red, and white bars on the scale are 0.1 m long. (A) Run 8, upper slope segment 8°, lower slope segment 0°; an experiment with a slope break and a horizontal lower-slope. Deposition created a ramp with an adverse gradient, which resulted in the formation of an upstream propagating roller structure. Camera 2 is facing the slope break showing the roller structure migrating upstream. (B) Run 14, upper slope segment 8°, lower slope segment 8°; an experiment setup with no slope break and a bypassing flow. (C) Run 2, upper slope 6°, lower slope 1°. An experiment with a slope break and a depositing flow. In both experiments, no roller structure was observed. Videos can be found in the supplementary material.

Video 1: Run 08, Camera 1. YouTube link: https://youtu.be/yKfQ15JFP0s

Video 2: Run 08: Camera 2. YouTube link: https://youtu.be/i8Wn2CDcQKo

Video 3: Run 14, Camera 1. YouTube link: https://youtu.be/5YMAYYqkAQA

Video 4: Run 02, Camera 1: YouTube link: https://youtu.be/uQERR6H4fKM